Fluid pressure arrival time tomography: Estimation and assessment in the presence of inequality constraints, with an application to a producing gas field at Krechba, Algeria

Alessio Rucci*, D. W. Vasco†, and Fabrizio Novali‡*

*Poletecnico di Milano, Italy
†Lawrence Berkeley National Laboratory, Berkeley, CA
‡TRE-Tele-Rilevamento Europa, Italy

ABSTRACT

Deformation in the overburden proves useful in deducing spatial and temporal changes in the volume of a producing reservoir. Based upon these changes we estimate diffusive travel times associated with the transient flow due to production, and then, as the solution of a linear inverse problem, the effective permeability of the reservoir. An advantage an approach based upon travel times, as opposed to one based upon the amplitude of surface deformation, is that it is much less sensitive to the exact geomechanical properties of the reservoir and overburden. Inequalities constrain the inversion, under the assumption that the fluid production only results in pore volume decreases within the reservoir. We apply the formulation to satellite-based estimates of deformation in the material overlying a thin gas production zone at the Krechba field in Algeria. The peak displacement after three years of gas production is approximately 0.5 cm, overlying the eastern margin of the anticlinal structure defining the gas field. Using data from 15 irregularly-spaced images of range change, we calculate the diffusive travel times associated with the start-up of a gas production well. The inequality constraints are incorporated into the estimates of model parameter resolution and covariance, improving the resolution by roughly 30 to 40%.

INTRODUCTION

The recent interpretation of some time-lapse seismic surveys indicates that oil and gas production can lead to stress changes and strain in the overburden (Barkved and Kristiansen 2005, Staples et al. 2005, Tura et al. 2005, Rickett et al. 2005, Roste et al. 2006). These studies complement earlier work on surface displacement and seismicity related to fluid pressure changes at depth (Castle et al. 1969, Segall 1985, Dussealt et al. 1993, Bruno and Bilak 1994, Fielding et al. 1998, Amelung et al. 1999, Massop and Segall 1999, Stancliffe and van der Kooij 2001, Schmidt and Burgmann 2003). Several investigations indicate that surface displacements can help in the estimation of reservoir pore volume and pressure changes associated with flow (Vasco et al. 1988, Mossop and Segall 1999, Vasco et al. 2000a, Du et al. 2005, Hodgson et al. 2007) and, ultimately, the effective permeability variations within the reservoir (Vasco et al. 2000a, Vasco and Ferretti 2005, Vasco et al. 2008)

In this paper we apply a modification of the inversion technique for diffusive arrival times described in Vasco et al. (2008). Their approach, formulated in terms of fluid pressure, is reformulated in terms of reservoir volume change. Inequality constraints are incorporated into the linear inverse problem for volume change within the reservoir. The inequality constraints are introduced to limit the tradeoff between positive and negative volume change in the model. The inequality follows from the expectation that gas production should lead to pore volume decreases within the reservoir. The application is to a set of Interferometric Synthetic Aperture Radar (InSAR) data gathered over a horizontal gas production well. The transient pore and fluid volume variations, constrained by the time-varying surface displacements, are modeled as a propagating front and analyzed using an asymptotic formulation similar to ray theory. A complete model assessment is conducted, both for the linear inverse problem and for the inverse problem with inequality constraints.

METHODOLOGY

Estimation of volume change, diffusive travel times, and effective permeability

One effect of any significant fluid extraction from a reservoir is that the reservoir, and subsequently the overburden can deform measurably over time. The goal of our work is to use such time-varying displacement to constrain reservoir flow properties, such as permeability. The first step in this approach consists of mapping the measured surface motion into reservoir pore and fluid volume changes (Vasco et al. 1988, Mossop and Segall 1999, Vasco et al. 2000a, Du and Olson 2001, Vasco and Ferretti 2005). In the second step, the temporal variations of the reservoir volume changes are used to construct diffusive travel times and to define flow path trajectories, as part of a tomographic inversion for permeability (Vasco et al. 2000b, Vasco et al. 2008).

Estimation of volume change

In this sub-section it is assumed that the reservoir volume has been discretized into a three-dimensional configuration of grid blocks. Each grid block within the reservoir can undergo a fractional volume change due to changes in fluid pressure induced by production. The set of fractional volume changes within the reservoir is denoted by the vector $\mathbf{v}$, where the i-th component of the vector represents the volume change of the i-th grid block. As described in detail in Vasco et al. (2000a) and Geertsma (1973) we can construct a linear system of equations relating the volume change at time t within each grid block of the reservoir model $\mathbf{v}(t)$ and the observed displacements at time t, $\mathbf{u}(t)$,

$$\mathbf{u}(t) = \boldsymbol{\Upsilon}\mathbf{v}(t) \tag{1}$$

where

$$\mathbf{v}(t) \leq \mathbf{0}.$$

The elements of the matrix $\boldsymbol{\Upsilon}_{ij}$ depend upon the Green's function which is the point response of the elastic medium at location of the j-th grid block $\mathbf{x}_j$ for the i-th data value (Vasco et al. 1988, Vasco et al. 2000a). We regularize the inverse problem with norm penalties and a penalty for volume change far from the well, as we expect that the largest volume and pressure changes will be at, or close to, the production well (Vasco and Ferretti 2005).

If the reservoir behaves elastically during each time interval, it is possible to map the volume change into fluid pressure using a technique described in Vasco et al. (2008), based upon the work of Segall (1985). Specifically, the fluid pressure changes are given by linear system of equations

$$\delta\mathbf{p}(t) = \boldsymbol{\Pi}\mathbf{v}(t) \tag{2}$$

which is just the forward problem, in which we map volume change $\mathbf{v}$ directly into fluid pressure change $\delta\mathbf{p}$. The coefficients of the matrix $\boldsymbol{\Pi}$ are given in Vasco et al. (2001).

Note that the mapping of volume change into pressure change, equation (2), depends upon the geomechanical properties of the reservoir and the overburden through the coefficients contained in the matrix $\boldsymbol{\Pi}$. Thus, the estimates of pressure change are limited by one's knowledge of the variations in the poroelastic parameters characterizing the reservoir. As shown below, lateral variations in reservoir properties can lead to errors in the estimates of the magnitude and pattern of pressure change. Seismic reflection data can provide information on variations in reservoir properties, such as porosity, and these data should be used if available.

Another important point is that, under certain circumstances, the change in fluid pressure at a point in the reservoir is linearly related to the volume change at that point. The conditions for this to hold are that the medium must behave elastically and the volumetric change due to the propagation of stress and displacement in the overburden and within the reservoir must be small relative to the volume change induced by the pressure change. If these conditions are satisfied, and the volume change is dominated by the local fluid pressure change, then the peak volume change will occur at the same time as the peak pressure change. Thus, even though the amplitude of the pressure change may be influenced by the coefficients in the matrix $\boldsymbol{\Pi}$, the arrival time, which is described below, will be relatively insensitive to the geomechanical properties contributing to the coefficient matrix. If the deformation deviates from linear elasticity then there may be a lag between the pressure change and any resulting volume change. For example, such a lag can occur due to visco-elastic behavior, as produced by the dewatering of shales (Liu and Helm 2008).

Estimation of the diffusive travel time and the fluid diffusivity

For a liquid, the equation governing the evolution of the fluid pressure within the reservoir is a form of the linear diffusion equation (de Marsily 1986). For gas the situation is somewhat more complicated due to the compressibility of the gas. That is, the density of a gas is a strong function of the gas pressure (Muskat 1946, Aronofsky and Jenkins 1954). Fortunately, there is an integral transformation from the physical pressure $p(\mathbf{x}, t)$ to a new variable $\hat{p}(\mathbf{x}, t)$ given by Al-Hussainy et al. (1966), where the transformed $\hat{p}$ variable satisfies a quasi-linear diffusion equation. Thus, when modeling gas we can work with the transformed variable and linearize the quasi-linear coefficient of the time derivative, the resulting equation is again a linear diffusion equation. The result is that a linear or quasi-linear diffusion equation may be used to model the flow of both gases and liquids.

As shown in Appendix A, using the linear relationship (2), we can write the equation for fluid pressure in terms of the induced volume change. Applying the Fourier transform to the resulting diffusion equation written in terms of the volume change $V(\mathbf{x}, t)$, gives [see equation (A9) in

Appendix A]

$$\Pi\nabla\cdot\nabla\hat{V}+\mathbf{\Psi}\cdot\nabla\hat{V}+\Omega\hat{V}=-\mathrm{i}\omega\Pi\kappa\hat{V} \tag{3}$$

where $V(\mathbf{x},\omega)$ is the Fourier transform of the volume change, $\mathbf{x}$ is the spatial coordinate, ω is the frequency,

$$\mathbf{\Psi}=\Pi\mathbf{\Lambda}+2\nabla\Pi,$$

$$\Omega=\nabla\Pi\cdot\mathbf{\Lambda}+\nabla\cdot\nabla\Pi$$

are coefficients that only depend upon $\mathbf{x}$, $\mathbf{\Lambda}=-\nabla\ln K(\mathbf{x})$ is the gradient of the logarithm of the absolute permeability $K(\mathbf{x})$, and

$$\kappa(\mathbf{x})=\frac{C_e(\mathbf{x})}{K(\mathbf{x})} \tag{4}$$

is the reciprocal of the fluid diffusivity (Vasco et al. 2000). The coefficient C_e, which can vary in space, relates fluid pressure variations to changes in porosity.

In Appendix A an asymptotic representation of the solution to the diffusion equation (3) is provided by a series in powers of $1/\sqrt{\omega}$

$$\hat{V}(\mathbf{x},\omega)=e^{-\sqrt{-i\omega}\sigma(\mathbf{x})}\sum_{n=0}^{\infty}\frac{A_n(\mathbf{x})}{(\sqrt{-i\omega})^n}. \tag{5}$$

Note that the zeroth-order term in equation (5)

$$\hat{V}(\mathbf{x},\omega)=A_0(\mathbf{x})e^{-\sqrt{-i\omega}\sigma(\mathbf{x})} \tag{6}$$

can be transformed back to the time domain, resulting in an expression

$$V(\mathbf{x},t)=A_0(\mathbf{x})\frac{\sigma(\mathbf{x})}{2\sqrt{\pi t^3}}e^{-\sigma^2(\mathbf{x})/4t} \tag{7}$$

that is very similar to the classic solution of the diffusion equation (Crank 1975). The function $\sigma(\mathbf{x})$ is referred to as the phase or the pseudo-phase function (Virieux et al. 1994) and is related to the propagation time of the transient diffusive disturbance. For an impulsive source-time function it can be shown that the phase $\sigma(\mathbf{x})$ is related to the arrival time of the pulse peak, T_{peak} (Virieux et al. 1994, Vasco et al. 2000):

$$\sigma=\sqrt{6T_{peak}}. \tag{8}$$

For a step-function source T_{peak} is the time as which the time derivative of the volume change $V(\mathbf{x},t)$ is a maximum (Vasco et al. 2000). Substituting this asymptotic series representation into the diffusion equation, and retaining terms of the lowest order in $1/\sqrt{\omega}$, (3) produces an eikonal equation

$$\nabla\sigma\cdot\nabla\sigma-\kappa(\mathbf{x})=0 \tag{9}$$

for the phase function $\sigma(\mathbf{x})$ [see Appendix A]. It is notable that the eikonal equation (9) implies that the phase only depends upon the flow properties and does not depend upon the reservoir compressibility $\Pi(\mathbf{x})$. This does make physical sense because, due to the linearity inherent in elastic deformation, both the peak and the peak rate of volume change occur at the same time as they do for the pressure change.

Expressing the eikonal equation in ray coordinates, we can write the phase function as an integral (Vasco et al. 2000b, Vasco et al. 2008)

$$\sigma(\mathbf{x})=-\int_{\mathbf{X}(l)}\sqrt{\kappa}dl \tag{10}$$

where $\mathbf{X}(l)$ is the trajectory from the production well to the point in the reservoir at which the volume change is being calculated or estimated. For a given set of phase values, corresponding to a set of arrival time constraints, each a discrete form of equation (10), can be written as a system of linear equations

$$\mathbf{\Sigma}=\mathbf{G}\mathbf{y} \tag{11}$$

where $\mathbf{\Sigma}$ is a vector of phase estimates, $\mathbf{G}$ is a coefficient matrix which contains the trajectory lengths in each grid block of the reservoir model, and $\mathbf{y}$ is a vector whose components are the average value of $\sqrt{\kappa}$ in each grid block (Vasco et al. 2000b).

Model parameter covariance estimation in the presence of inequality constraints

Due to the presence of inequality constraints in equation (1), the inverse problem, in which we solve for the reservoir volume change $\mathbf{v}$, is no longer linear. Thus, techniques from linear inverse theory for the assessment of model parameter estimates (Parker 1994) are not necessarily accurate. In this paper we present three different approaches to evaluate model parameter variance and the covariance matrix for an inverse problem subject to inequality constraints. As discussed below, each approach is approximate and each has specific strengths and weaknesses. The first method, based upon Monte Carlo simulation, is the simplest and the most widely used technique. The second technique, which is original, leads to an analytical approximation of the posteriori model parameter variance. The third approach, first developed by Liew (1976a, 1976b), approximates the covariance matrix associated with the constrained least squares problem using an implicit linearization.

Covariance estimation for the linear inverse problem

Before presenting the three approaches, we briefly discuss the covariance matrix associated with a linear inverse problem. That is, let us consider the linear problem specified in equation (1), without the additional inequality constraints. The linear inverse problem, given by the set equality constraints in equation (1), has a solution

$$\hat{\mathbf{v}}=\mathbf{\Upsilon}^{\dagger}\mathbf{u} \tag{12}$$

where $\hat{\mathbf{v}}$ are the estimated volume changes, $\mathbf{\Upsilon}^{\dagger}$ is the generalized inverse of the matrix $\mathbf{\Upsilon}$, which may include regularization components if the problem is ill-conditioned and

hence the matrix $\boldsymbol{\Upsilon}$ is singular (Aki and Richards 1980, Menke 1984, Parker 1994, Tarantola 2005). Because, as indicated in equation (1), the model parameter estimates $\hat{\mathbf{v}}$ are linearly related to the data $\mathbf{u}$, one can show that the posteriori covariance matrix is given by

$$\mathbf{C}_{vv} = \left(\boldsymbol{\Upsilon}^{\dagger}\right)^{T} \mathbf{C}_{uu} \boldsymbol{\Upsilon}^{\dagger} \tag{13}$$

where $\mathbf{C}_{vv}$ and $\mathbf{C}_{uu}$ represents the model parameter and the data covariance matrices, respectively (Aki and Richards 1980, Menke 1984).

Covariance estimation via Monte Carlo simulation

Monte Carlo simulation is a very general approach for solving inverse problems (Press 1968, Tarantola 2005). The technique also allows one to estimate the model parameter covariance matrix through the successive inversions of data plus additive noise (Tarantola 2005). The noise is modeled as random deviates with a prescribed statistical structure representing the errors associated with the observations. The perturbed observations are inverted with the same algorithm used to invert the actual observations. Given an extensive set of inversion results it is possible to evaluate the sampled covariance matrix directly from the resulting suite of models. Unlike the linear formulation, in the presence of inequality constraints the covariance matrix depends upon the model values. For this reason, when conducting the Monte Carlo simulation, we add noise to the displacement predicted by the estimated model of volume change. That is, we invert the simulated displacements for the i-th set of values $\mathbf{u}_i$, given by

$$\mathbf{u}_i = \boldsymbol{\Upsilon}\hat{\mathbf{v}} + \boldsymbol{\Gamma}_i \tag{14}$$

where $\boldsymbol{\Gamma}_i$ is a vector of random deviates with the same statistical properties as the data errors.

Estimation of variance based upon statistical moments

As the Monte Carlo methodology may be computationally intensive, a different approach is desirable for large-scale models with numerous parameters. A more efficient technique follows from an analytical approximation of the model parameter variance, based upon the first two statistical moments of the underlying probability distribution function. Due to the inequality constraints, a gaussian distribution is not mapped into an a posteriori gaussian distribution. Thus, even if the errors in the data are normally distributed, the model parameter estimates will not necessarily be normally distributed. In particular, constrained least squares algorithms have a tendency to map negative model parameter estimates to the origin, increasing the frequency of zero estimates for these parameters. This phenomena has been noted in the statistical literature and observed in the Monte Carlo-based analysis of positively constrained inverse problems (Vasco et al. 1990).

For a univariate view along one axis, we approximate the probability distribution by the linear combination of a delta-function at zero and a truncated gaussian distribution (Johnson and Kotz 1970). The delta-function is scaled such that its integrated area is equal to the area under the 'missing' portion of the gaussian which lies to the right of the origin in the case of a negativity constraint. In this statistical model, the probability density function, for the i-th parameter, representing the volume change of the i^{th} grid block, v_i, is given by

$$\begin{aligned} \mathrm{pdf}_{v_i}(v) = \frac{1}{2}\left[1 + \mathrm{erf}\left(\frac{\mu_i}{\sqrt{2\sigma_i^2}}\right)\right]\delta(v) + N(\mu_i,\sigma_i)H(-v) \\ v \leq 0 \end{aligned} \tag{15}$$

where μ_i and σ_i represents respectively the mean and the standard deviation of the i-th element of the unconstrained model parameter vector, $N(\mu_i,\sigma_i)$ is the associated gaussian distribution, and $H(v)$ is the Heaviside step-function, representing a unit step at the origin. After some algebra we can evaluate the mean value, θ_i, for the probability distribution function (15)

$$\begin{aligned} \theta_i &= \int_{-\infty}^{+\infty} v \cdot \mathrm{pdf}_{v_i}(v)dv \\ &= \frac{\sigma_i}{2}\left[-\exp\left(-\frac{\mu_i^2}{2\sigma_i^2}\right)\sqrt{\frac{2}{\pi}} + \frac{\mu_i}{\sigma_i} - \frac{\mu_i}{\sigma_i}\mathrm{erf}\left(\frac{\mu_i}{\sqrt{2\sigma_i^2}}\right)\right]. \end{aligned} \tag{16}$$

Using expression (16) for the mean value, we next compute the variance, $\vartheta(v_i)$, again by direct integration

$$\begin{aligned} \vartheta(v_i) &= \int_{-\infty}^{+\infty} (v-\theta_i)^2 \cdot \mathrm{pdf}_{v_i}(v)dv \\ &= \frac{1}{\sqrt{2}}[(\mu_i - 2\theta_i)^2 + \sigma_i^2]\mathrm{erfc}\left(\frac{\mu_i}{\sqrt{2\sigma_i^2}}\right) \\ &+ \theta_i^2\frac{1}{2}\left[1 + \mathrm{erf}\left(\frac{\mu_i}{\sqrt{2\sigma_i^2}}\right)\right] \\ &- \frac{1}{\sqrt{2\pi}}\exp\left(-\frac{\mu_i^2}{2\sigma_i^2}\right)(\mu_i - 2\theta_i)\sigma_i. \end{aligned} \tag{17}$$

In expression (17), the statistical parameters associated with the truncated normal distribution, μ_i and σ_i, are approximated by the model parameter mean and standard deviation calculated for the solution of the unconstrained linear inverse problem. That is, we first solve the linear inverse problem, using the generalized inverse [see equation (12)]. From the solution of the linear inverse problem we obtain the mean of model parameter and, using the expression (13), find the standard deviation. Substituting these values into expression (17) provides an estimate of the model parameter variance associated with the inverse problem containing inequality constraints. Using this procedure, we obtain an analytic approximation of the model parameter variance.

Inequality constrained least squares estimation

As noted by Gill et al. (1981), the least squares solution of equation (1) is equivalent to a quadratic programming problem, in which one minimizes a quadratic function

$$\min \left\{ (\mathbf{u} - \boldsymbol{\Upsilon}\mathbf{v})^T \cdot (\mathbf{u} - \boldsymbol{\Upsilon}\mathbf{v}) \right\} \tag{18}$$

subject to linear inequality constraints

$$A\mathbf{v} \geq \mathbf{0}.$$

In equation (1) we have the simple requirement that the volume changes are negative, resulting in $\mathbf{A} = -\mathbf{I}$. There are well developed computational procedures for solving the quadratic programming problem, as noted in Appendix B. Many of the algorithms have been influenced by the highly successful approach to linear programming developed by Dantzig (Hadley 1962).

Based upon the solution procedure for the quadratic programming problem, discussed in Appendix B, we can relate the solution of the constrained least squares problem, given above and denoted by $\mathbf{v}_c$, and the solution of the unconstrained least squares problem ($\hat{\mathbf{v}}$) [equation (12)]. Specifically, one can derive a linear relationship between the unconstrained least squares solution and the solution with inequality constraints

$$\mathbf{v}_c = \mathbf{Q}\hat{\mathbf{v}} \tag{19}$$

where

$$\mathbf{Q} = [\mathbf{I} - (\boldsymbol{\Upsilon}^T\boldsymbol{\Upsilon})^{-1}\mathbf{I}_2\mathbf{M}_2] \tag{20}$$

(Liew 1976a, 1976b), the matrices $\mathbf{I}_2$ and $\mathbf{M}_2$ are defined in Appendix B. Given the apparent linear relationship between the two solutions, there is a direct mapping between the covariance matrix of the unconstrained solution, $\mathbf{C}_{vv}$ and the covariance matrix of the constrained solution $\mathbf{C}_{v_cv_c}$

$$\mathbf{C}_{v_cv_c} = \mathbf{Q}\mathbf{C}_{vv}\mathbf{Q}^T. \tag{21}$$

Note that, the matrices $\mathbf{I}_2$ and $\mathbf{M}_2$ depend upon the final solution and so the matrix $\mathbf{Q}$ is actually a function of the data and the covariance estimates are only approximate.

Estimating the model parameter resolution matrix for an inverse problem with inequality constraints

Due to errors in the observations and the instability associated with most inverse problems it is generally not possible to estimate the properties of the Earth exactly. Rather, one typically must incorporate some form of regularization into the inversion which biases the results in some fashion. The idea of a resolution matrix is to try and estimate the blurring that is inherent in a regularized inversion. In essence, the resolution matrix relates model parameter estimates obtained by solving the regularized inverse problem, to a hypothetical 'true' model that satisfies the error free forward problem exactly.

Resolution in the case of a linear inverse problem

The resolution matrix arose in the study of linear inverse problems and that is where we begin our discussion. Consider a solution of the unconstrained linear inverse problem, $\hat{\mathbf{v}}$, given in terms of the generalized inverse, $\boldsymbol{\Upsilon}^\dagger$, appearing in equation (12). The resolution matrix is obtained by substituting for $\mathbf{u}$ in equation (12) using the linear equations (1). The result is a relationship between our model parameter estimates $\hat{\mathbf{v}}$ and a model $\mathbf{v}$ that would reproduce the data exactly

$$\hat{\mathbf{v}} = \boldsymbol{\Upsilon}^\dagger\boldsymbol{\Upsilon}\mathbf{v}. \tag{22}$$

The matrix relating the two solutions

$$\mathbf{R} = \boldsymbol{\Upsilon}^\dagger\boldsymbol{\Upsilon} \tag{23}$$

is the formal resolution matrix (Aki and Richards 1980, Menke 1984, Parker 1994). The rows of the resolution matrix (23) are averaging coefficients, indicating the contribution of all model parameters to the model parameter estimate. For a perfectly resolved model the resolution matrix would be an identity matrix. A diagonal value near 1 means that it is possible to estimate the parameter with little tradeoff from any other parameter. Conversely, small diagonal values mean that we cannot estimate that particular parameters in isolation from the other parameters.

A purely numerical estimate of resolution

The inequality constraints in equation (1), render the inverse problem nonlinear. Hence, we cannot solve it using a generalized inverse, as in equation (12), and the formulation (22) cannot be used directly. However, it is still possible to construct a resolution matrix using a purely numerical approach. If we consider the data generated by a model vector $\mathbf{v}_m$ whose elements are zero, with the exception of the m-th element, which is equal to one, then the resulting solution, $\hat{\mathbf{v}}_m$, of the constrained inverse problem gives a column of the resolution matrix: (Humphreys and Clayton, 1988)

$$\hat{\mathbf{v}}_m = \mathbf{R}\mathbf{v}_m = \mathbf{R}_m. \tag{24}$$

where $\mathbf{R}_m$ is m-th column of the resolution matrix. So to infer the resolution matrix for the constrained inverse problem we have to generate synthetic data corresponding to the $\mathbf{v}_m$ model vector, for each m, and solve the corresponding inverse problem. Thus, for N model parameters we must conduct N inversions, which might involve considerable computation for a large problem.

An approximate estimate of the resolution matrix for inequality constrained least squares problems

An alternative estimate of the resolution matrix follows from the work of Liew (1976a, 1976b) for the least squares problem with inequality constraints. In particular, we

may combine the relationship (19) with the linear estimate given by equation (22) to relate the solution of the constrained problem $\mathbf{v}_c$ to the hypothetical 'true' solution

$$\mathbf{v}_c = \mathbf{Q}\boldsymbol{\Upsilon}^\dagger\boldsymbol{\Upsilon}\mathbf{v}. \quad (25)$$

We can define the resolution matrix for the constrained problem, $\mathbf{R}_c$ as

$$\mathbf{R}_c = \mathbf{Q}\boldsymbol{\Upsilon}^\dagger\boldsymbol{\Upsilon}. \quad (26)$$

As with the covariance matrix, given by equation (21), this estimate is approximate because the matrix $\mathbf{Q}$ depends upon the observations.

APPLICATION

The In Salah gas storage project at the Krechba field, Algeria

Overview

Geologically, the Krechba field is part of a large structural anticline, capped by approximately one kilometer of Carboniferous mudstone. The mudstone is, in turn, overlain by a kilometer of interbedded sandstones and mudstones. The anticline is intersected by several fault and fracture systems which complicate the geology. The reservoir itself is rather thin, roughly 20 m thick, and of variable quality. Natural gas is extracted from the reservoir via a set of horizontal wells which are distributed along the crest of the anticline. The natural gas from the field contains excess CO_2 which is separated from the hydrocarbons and reinjected at the flanks of the gas field.

The In Salah Gas storage project represents one of the first CO_2 sequestration efforts associated with an active gas reservoir. Due to this sequestration effort, roughly 1 million metric tons of CO_2 are prevented from entering the atmosphere each year. The In Salah project in Algeria, along with the Sleipner field in the North Sea (Arts et al. 2004), and the Weyburn project in Canada (White et al. 2004) represent the first large-scale CO_2 storage projects currently operating worldwide. The satellite data, described next, were primarily gathered to monitor the CO_2 injection of the In Salah Gas storage project. However, it was noted that subsidence related to the gas production, that commenced somewhat before the injection of the carbon dioxide, was also observable.

Monitoring surface displacement due to injection and production

For our study we utilize descending-orbit satellite radar images of the European Space Agency's Envisat archive from July 12, 2003 through March 19, 2007. The satellite reflects radar waves off of the surface of the Earth and records their return as a complex trace. Phase shifts between repeat reflections are related to variations in range, which is the distance between the reflection point on the Earth and a reference point in space. Two satellite paths, tracks 65 and 294, traversed the production and injection region during this time period, producing 26 and 19 images, respectively (Vasco et al. 2008). The range changes from the two tracks have been re-interpolated onto a sequence of 15 irregularly spaced snapshots [0, 24, 58, 96, 128, 159, 198, 265, 306, 408, 545, 586, 677, 728 and 842 days]. The data were processed by Tele-Rilevamento Europa (TRE) using the Permanent Scatterer InSAR (PSInSAR^{TM}) technique. PSInSAR^{TM} is a multi-image technique able to estimate and remove the atmospheric noise, providing range change estimates with millimeter accuracy (Ferretti et al. 2000,2001). In Figure 1 four images of range change, obtained by combining the observations from tracks 65 and 294, are shown. At 842 days we observe a peak subsidence of about 0.5 centimeters, offset somewhat to the east from the three main production wells, shown as horizontal lines in the figure.

Estimation of reservoir volume change due to production

To infer flow properties, such as the effective permeability, within the reservoir we use the approach outlined in the Methodology section. The first step entails inverting the observed surface displacement for reservoir volume change. One difficulty associated with this field is that the three production wells (KB−11, KB−12 and KB−14) are in close proximity and went on-line at approximately the same time. Thus, their transient pressure fields rapidly began to interfere. Due to this interference, we have limited our analysis to a region surrounding the well that started first: KB−11.

For our analysis the 20 m reservoir interval is sub-divided into a 15 by 15 grid of blocks, each about 600 m in lateral extent. The top of the reservoir was determined from a seismic reflection survey and used to define the vertical boundaries of each grid block (Figure 2). Following the procedure mentioned above, and described in more detail in Vasco et al. (2008), we formulated an inverse problem for reservoir volume change. The green's functions correspond to a layered medium, as described in Vasco et al. (2010). This model, which is based upon well logs, is judged to be an adequate representation of the relatively flat-lying overburden. Both model norm regularization and a penalty term proportional to the distance from the extraction well:

$$R = |\mathbf{u} - \boldsymbol{\Upsilon}\mathbf{v}|_2 + W_d|D\mathbf{v}|_2 + W_n|\mathbf{v}|_2 \quad (27)$$

are included in the inversion. In the expression (27) $|\mathbf{v}|_2$ signifies the L_2 norm of the vector $\mathbf{v}$, D is a distance weighting function defining the distance penalty, W_d is the weight associated with the distance penalty, and W_n is the weight associated with the norm regularization. The distance penalty term is an attempt to ensure that the largest reservoir volume changes, that are thought to be due to pressure changes in the reservoir, should be at or near the production well. Note that, due to spatial variations in reservoir properties such as compressibility and

porosity, there may be large volume changes some distance from the production well. In fact, we do observe that the peak range changes do not occur over the production wells (Figure 1). Rather, we find that the greatest range change is offset to the east of the production wells by a kilometer or more.

We further hypothesize that, within the reservoir zone the pore volume changes will be dominated by pressure decreases due to gas production. To enforce this, we incorporate inequality constraints in addition to the linear data constraints [equation (1)]. To solve the linear system subject to inequality constraints, we use a reflective Newton method (Coleman et al. 1996, Gill et al. 1981) suitable for large-scale problems, where a quadratic function has to be minimized subject to bounds. For comparison, we also solve the inverse problem without imposing inequality constraints on the solution. To solve this problem (1), we use a pre-conditioned conjugate gradient solver (Barrett et al. 1994) known for its rapid convergence. In Figures 3 and 4 we show the inferred volume changes for four time intervals [96, 198, 408, and 842 days], that are solutions of the unconstrained and the constrained inverse problems, respectively. The two solutions are very similar in character, with the peak volume change lying to the east of the three production wells, at the edge of the anticline that defines the gas field. However, the inequality constraints do indeed eliminate the positive and negative trade-offs that are observed in the unconstrained solutions (Figure 3).

Model parameter resolution estimates

Including inequality constraints in the inverse problem means that is no longer possible to provide analytic expressions for either the resolution or the covariance matrix. However, inequality constraints can produce a more plausible solution, for example, eliminating significant volume increase in a producing horizon. Furthermore, inequality constraints can remove trade-offs between cells, such as adjacent positive and negative volume changes, which add to the non-uniqueness associated with the inverse problem. Thus, inequality constraints can reduced uncertainty and improve model parameter resolution.

In Figure 5 we present the diagonal elements of resolution matrix for the unconstrained inverse problem. For a well resolved model, the diagonal elements should approach unity, indicating that the estimates do not trade-off in value. The rows of the resolution matrix are useful in quantifying the spatial averaging associated with a particular model parameter estimate. Consider the j-th row of the resolution matrix, the value of each element of the row indicates the contribution of the corresponding unknown to the estimate of the j-th unknown. As is evident in diagonal elements, shown in Figure 5, the peak values of the diagonal elements do not exceed 0.2 in magnitude. The results suggest that, even though our model consists of a single layer, there may be considerable trade-offs between the estimates of volume change in adjacent grid blocks. We can verify the existence of such trade-offs if we examine the rows of the resolution matrix, which are averaging coefficients, as in Figure 6. The four rows of the resolution matrix, shown in Figure 6, indicate significant averaging with the volume change estimates over a radius of about 2 Km.

When inequality constraints are included in the inverse problem we have to use either a numerical approach or the approximation (26) to evaluate the resolution matrix. In this study we used the numerical approach, given by equation (24), which requires one complete inversion for each model parameter to estimate the exact resolution matrix. We plot the diagonal elements and four rows of the resolution matrix in Figures 7 and 8, respectively. When inequality constraints are present, the size of the diagonal elements of the resolution matrix increase by roughly 40 percent. The individual rows of the resolution matrix are more sharply concentrated about the point of interest (Figure 8) and do not contain the negative trade-offs that are seen in Figure 6.

Model parameter variance estimates

Our estimates of volume change are based upon the inversion of the range change observations (Figure 1). Because the range change measurements contain errors, our estimates of volume change will also contain some level of error. For a linear inverse problem, one without inequality constraints, there is a direct mapping from the covariance matrix associated with the observations and the covariance matrix of the model parameters, given by equation (13). Though we do not have enough redundancy in our range change estimates to construct a statistical model of the data errors, we can approximate an error model. To construct an approximate data covariance matrix we considered two types of gaussian noise: spatially uncorrelated noise, representing random noise at each measurement point, and a spatially correlated noise associated with an atmospheric noise component of the SAR data. The standard error on the range change observations is of the order of about one millimeter, that is the expected accuracy for PSInSAR^{TM}. The diagonal elements of the resulting model parameter covariance matrix, given by the mapping (13), based upon the estimated data covariance, are shown in Figure 9.

If we include inequality constraints we can apply the three techniques introduced in the Methodology section to approximate the model parameter variance. The first method, based upon Monte Carlo simulation, is rather time-consuming because of the large number of simulations required to guarantee convergence. Figure 10 displays the diagonal elements of the sampled model parameter variances, estimated from 350 distinct inversions. The standard deviations in Figure 10 are generally lower than those associated with the linear problem, except for a few regions. These regions appear to lie at boundaries between areas where there is significant range change and areas where there is little recorded range change.

Due to the presence of inequality constraints, second-order statistics such as the variance, do not give a complete description of the parameter probability distribution. Furthermore, due to the non-linearity of the inverse problem, the gaussian nature of the data errors does not imply that the model parameter estimates will be gaussian. Consider, for example, Figure 11 in which we present four probability density functions (pdf) computed using the 350 inversions from the Monte Carlo simulation. We ran two sets of inversions: one with inequality constraints and one without inequality constraints. As noted by others, the constrained pdfs appear to consist of a combination of a gaussian truncated at zero and a spike centered at zero. These results support our heuristic construction of the pdf given by equation (15), which is the basis for our second method. We used this method to estimate the variance for each model parameter, as given by equation (17). The parameters μ_i and θ_i in equation (17) were taken from the results of the unconstrained inversion. The standard deviations, computed using equation (17), are shown in Figure 12. Note that they are similar to the Monte Carlo estimates shown in Figure 10.

The final approach, expressed mathematically by equations (19), (20), and (21), provides an analytical approximation for the entire covariance matrix. Thus, we compute the first and second statistical moments of the distribution but not the higher-order properties. As noted above, in this approximation of the covariance, the matrix $\mathbf{Q}$ depends upon the data and so the estimates are approximate. For this reason, to have a fair comparison with the previous approaches, we decided to use equation (14) to evaluate the covariance matrix for each Monte Carlo realization and then we average the realizations. In Figure 13 we show the diagonal elements of the estimated covariance matrix. In Figure 14 we cross-plot the the standard deviation estimates obtained by an approximation of the pdf [equation (15)] and its moments against the standard deviation estimates from the covariance matrix for the constrained least squares estimation [equation (21)]. We see a positive correlation between the two estimates, one that is supported by a visual comparison of Figures 12 and 13.

Estimation of reservoir pressure change and diffusive travel time

Given estimates of the volume changes within the reservoir it is possible to map them into reservoir pressure changes using Equation (2). While such a mapping is helpful in trying to understand the evolution of pressure due to the start of production, it is not necessary in order to estimate the diffusive travel time. As noted above, we can estimate the phase and travel times directly from the volume changes themselves.

The matrix, $\mathbf{\Pi}$, for mapping volume change into pressure change contains two contributions: the first provides a direct elastic relationship between volume and pressure change associated with a given grid block, the second is due to the propagation of the stress within the reservoir and the overburden which couples different grid blocks (Segall 1985, Vasco et al. 2001). Numerical testing indicates that the contribution from the propagation of stress is second-order in importance. Thus, the relationship between volume change in pressure change can be adequately approximated by the mapping

$$\delta p(\mathbf{x}, t) = \frac{1}{\beta(\mathbf{x})} v(\mathbf{x}, t) \tag{28}$$

where $\beta(\mathbf{x})$ is a proportionality coefficient (Vasco et al. 2008). The coefficient β represents the compressibility of the material, a measure of the relative volume of a fluid or solid in response to a change in pressure.

Note that equation (28) assumes linear elastic behavior during the time interval of interest. Some materials, particularly clays and shales can deform visco-elastically, introducing a time lag between the pressure change and the volume change. There is certainly an abundance of shale in the overburden which will deform inelastically. However, we are only considering up to 842 days of deformation. A Study of phase lags between volume change and pressure change in relatively unconsolidated clays (Liu and Helm 2008) indicates that the time shift start to behave inelastically after about 900 days. We expect that the consolidated shales at Krechba will take even longer than this to begin deforming inelastically. Thus, over the time interval of 842 days, we expect that the relationship between pressure change and volume change is adequately described by equation (28).

We found that assuming a spatially homogeneous compressibility within the reservoir produces unrealistic estimates of pressure change. In particular, using homogeneous mechanical properties results in a peak in pressure change that is removed from the producing well, offset by a kilometer or more to the east (Figure 15). In most cases, such offsets in peak pressure are not physically plausible, suggesting that a homgeneous geomechanical model is inadaquate for mapping volume change to pressure. For this reason we have attempted to estimate a spatially-varying compressibility within the reservoir. The idea underlying our estimate is to try and use the volume changes at the later intervals as a measure of the compressibility of the reservoir. During the later time intervals the rapid pressure variations associated with the onset of production should have propagated out beyond the region of interest. We can use the estimates of diffusive travel time to verify that this is indeed true. Thus, at these later times, the pressure changes over the region of study should vary relatively slowly as a function of space and time. We approximate the pressure change for one of the later time intervals as constant over the region. Then we use the ratio of volume change to the constant pressure change as a measure of the compressibility. This is a crude approximation, however, as we lacked access to detailed reservoir data, it was not possible to provide a better estimate. We felt that the approach was preferable to simply assuming a constant compressibility for the reservoir which gives an

implausible pressure distribution (Figure 15).

So, as a first step, we estimate the diffusive travel time in an effort to discern the time after which the pressure transient has propagated beyond the region under study. From the time sequence of volume changes we estimated the propagation time for the disturbance generated by the initiation of pumping at well KB-11. In order to estimate the arrival time in each grid block, we find the time at which there is a peak in the derivative of the pressure time series for each grid block. As noted above, one advantage of the travel time formulation is that, if the pressure is proportional to the volume change, as in equation (28), the estimated arrival time is not sensitive to the exact value of compressibility at a particular grid block. Because the production rate was not a step function but had several peaks and troughs, there are corresponding peaks and troughs in the time series of the estimated pressure changes. We considered the arrival time corresponding to the first observable peak. The resulting travel time estimates are shown in Figure 16.

Even though well KB-11 was the first to initiate pumping, well KB-12 began pumping only 50 days later. Thus, the pressure field to the south of the well is influenced by the activity at KB-12, forcing us to truncate the pressure arrival time estimates roughly mid-way between the wells. This truncation is evident in Figure 16, where we have plotted the square root of the diffusive travel time estimates. From the travel time estimates (Figure 16), it seems that the pressure change has propagated to the edge of the region after about 625 days (25×25). So we used the volume changes between 728 and 842 days to infer the relative compressibility within the reservoir. Thus, assuming that the pressure change behind the diffusive front, and away from the pumping well, is slowly varying and may be approximated as a constant pressure change, the relative compressibility is calculated using:

$$\beta(\mathbf{x}) = \frac{v(\mathbf{x})}{\overline{\delta p}} \tag{29}$$

where $\overline{\delta p}$ is the spatially averaged pressure change between 728 and 842 days.

Given the spatially varying compressibilities from equation (29), we can compute the pressure changes for each of the 15 time intervals using equation (2). Alternatively, we can combine equations (1) and (2) and solve directly for the pressure change in terms of the range change. For this inversion we included regularization that penalizes pressure changes that are far from the production well. The resulting pressure changes are shown in Figure 17. Taking into account the spatial heterogeneity in compressibility we get now a plausible solution for pressure change, with a peak pressure changes close to the well. As before, from the new pressure estimates for each grid block we can calculate diffusive travel times to each grid block (Figure 18). Note the similarity to the diffusive travel time computed without accounting for the variation in geomechanical properties (Figure 16). The similarity of the travel times validates the expression for the phase of the volume change, equation (9), that indicates that the diffusive arrival times are not sensitive to the compressibilities within the reservoir. So, while the pressure amplitude estimates are sensitive to spatial variations in the poroelastic properties of the reservoir (Figure 15 and Figure 17), the pressure arrival time estimates are not (Figure 16 and Figure 18).

Estimation of effective permeability

Given the pressure arrival times, which are not sensitive to the compressibility variations within the reservoir, we can now estimate the effective permeability within the reservoir. First, we discretize the reservoir into a rectangular grid of cells. Using the arrival times we define a phase field over the entire grid. Following the procedure described in Vasco et al. (2008), which is essentially a raytracing algorithm, we compute trajectories $\mathbf{X}(l)$ from the producing well to each mesh point. In Figure 19 we plot the trajectories connecting each of the grid blocks to the production well. Given the trajectories, and an estimate of the C_e [see equation (4)] for the region, we can determine the effective permeability in each grid block of the reservoir model by solving equation (11) for $\sqrt{\kappa}$ in each grid block. Because of errors in the data and modeling approximations, we adopt a penalized least square approach, with roughness penalties, minimizing

$$R = |\mathbf{\Sigma} - \mathbf{G}\mathbf{y}|_2 + W_r|\mathbf{D}\mathbf{y}|_2 \tag{30}$$

where W_r is a scalar coefficient controlling the importance of the penalty terms in relation to the importance of fitting the data, and $\mathbf{D}$ is a matrix which approximates the Laplacian operator (Menke 1984). The coefficient matrix $\mathbf{G}$ [see equation (11)] is defined in terms of the trajectories shown in Figure 19 (Vasco et al. 2008).

The effective permeabilities, inferred from the penalized least squares solution are plotted in Figure 20. The solution was constrained by the range change data and by inequality constraints. The permeability estimates contain two high permeability regions. The two high permeability anomalies lie beneath the area with the largest observed range change (Figure 1). This region lies somewhat to the east of the three production wells, at the eastern edge of the anticline defining the gas field. One of the high permeability features is aligned in the direction of the regional fault system, suggesting that it might be a fracture. The second anomaly coincides with a large depth variation in the topography of the reservoir (Figure 2).

DISCUSSIONS AND CONCLUSIONS

Deformation and strain above a producing reservoir can provide information related to fluid flow within the reservoir. Such displacement can often be measured by geophysical techniques, such as ocean-bottom pressure sensors, or by time-lapse seismic observations. Because we

are using data gathered at some distance from the reservoir, the technique generally reproduces the low resolution component of reservoir volume change. However, as shown above, we can map such volume changes into large-scale permeability variations in a reservoir. Using measurements of surface displacement near to the reservoir, as provided by time-lapse seismic strain data, might improve the spatial resolution of the volume changes. If the reservoir behaves elastically during the initiation of pumping, the travel time inversion methodology is much less sensitive to the geomechanical properties of the reservoir than is a direct inversion for pressure amplitudes. With the exception of the inequality constraints, the inversion for permeability is linear leading to efficient algorithms. In this study we only considered a single component of deformation, range change along the line-of-sight to the satellite. Numerical simulations indicate that if two components of displacement were available, horizontal and vertical, the resolution would improve by an additional fifty percent. Such multi-component data will be the focus of a future investigation.

The inclusion of inequality constraints leads to an improvement of approximately 40% in the resolution of the estimated volume change model. We have presented three different approaches for estimating the posteriori model parameter variance in the presence of inequality constraints. The three techniques give similar variance estimates and these values differ notably from linear estimates. The algorithms described in this paper are applicable to a wide variety of data: sea-floor pressure sensors, tilt meters, time-strains from time-lapse seismic observations, Global Positioning System data, as well as the InSAR data discussed here. The permeability estimation may be used in conjunction with methods for measuring pressure change, for example the direct imaging of pressure change by time-lapse seismic monitoring or electromagnetic data sensitive to the location of the water table. Furthermore, the model assessment techniques, for calculating resolution and covariance, could prove useful for a wide array of problems in which the unknowns are restricted in sign.

ACKNOWLEDGMENTS

This work was supported by the Assistant Secretary, Office of Basic Energy Sciences of the U. S. Department of Energy under contract DE-AC02-05CH11231. The permanent scatterer data were processed by Tele-Rilevamento Europa (TRE). The authors wish to thank the European Space Agency for all satellite data used in this study and the entire TRE staff for supporting the SAR data processing. The In Salah CO_2 Joint Industry Project (BP, StatoilHydro, and Sonatrach) is thanked for provision of production, injection, and subsurface data.

APPENDIX A: AN ASYMPTOTIC EXPRESSION FOR THE RESERVOIR VOLUME CHANGE

In this Appendix we demonstrate that one can relate the phase or pseudo-phase associated with the volume change to the flow properties of the medium. Thus, as discussed in Vasco et al. (2000) and noted in the body of the text, we can relate the time at which rate of volume change is a maximum to the fluid diffusivity. As shown below, the expression is identical to that for the fluid pressure and independent of the geomechanical properties of the reservoir layer.

We begin with the governing equation for fluid pressure $P(\mathbf{x},t)$ in the reservoir

$$\nabla \cdot (K \nabla P) = C_e \frac{\partial P}{\partial t} \tag{A1}$$

where $K(\mathbf{x})$ is the absolute permeability and $C_e(\mathbf{x})$ is the coefficient relating fluid pressure variations to changes in porosity. Assuming elastic behavior over the monitoring interval, generally one year or a few years, and assuming that the bulk of the volume change is due to fluid pressure changes in the reservoir, we relate the fluid pressure to the volume change $V(\mathbf{x})$ as

$$P(\mathbf{x},t) = \Pi(\mathbf{x}) V(\mathbf{x},t) \tag{A2}$$

as given above [equation (2)]. Substituting the expression (A2) for $P(\mathbf{x},t)$ in the governing equation (A1) gives

$$\nabla \cdot [K \nabla (\Pi V)] = C_e \Pi \frac{\partial V}{\partial t} \tag{A3}$$

an equation for the volume change $V(\mathbf{x},t)$. Expanding the gradient and divergence operators gives

$$\nabla K \cdot (V \nabla \Pi + \Pi \nabla V) + K \nabla \cdot (V \nabla \Pi + \Pi \nabla V) = C_e \Pi \frac{\partial V}{\partial t}. \tag{A4}$$

Dividing through by $K(\mathbf{x})$, defining

$$\mathbf{\Lambda} = -\nabla \ln K, \tag{A5}$$

and grouping terms gives

$$\Pi \nabla \cdot \nabla V + \mathbf{\Psi} \cdot \nabla V + \Omega V = \Pi \frac{C_e}{K} \frac{\partial V}{\partial t}, \tag{A6}$$

where

$$\mathbf{\Psi} = \Pi \mathbf{\Lambda} + 2 \nabla \Pi \tag{A7}$$

and

$$\Omega = \nabla \Pi \cdot \mathbf{\Lambda} + \nabla \cdot \nabla \Pi \tag{A8}$$

are coefficients that only depend upon $\mathbf{x}$. Taking the Fourier transform (Bracewell 1978) of equation (A6) produces the partial differential equation

$$\Pi \nabla \cdot \nabla \hat{V} + \mathbf{\Psi} \cdot \nabla \hat{V} + \Omega \hat{V} = -\mathrm{i} \omega \Pi \frac{C_e}{K} \hat{V} \tag{A9}$$

where $\hat{V}(\mathbf{x},\omega)$ is the Fourier transform of $V(\mathbf{x},t)$.

We are interested in those components of transient volume change associated with the initiation of production. Typically, such transient behavior is much more rapid then the natural background variation in volume change. In order to isolate the signal of interest, that associated with the start of production, we shall represent the solution of equation (A8) as a series in inverse powers of the frequency ω

$$\hat{V}(\mathbf{x},\omega) = e^{-\sqrt{-i\omega}\sigma(\mathbf{x})} \sum_{n=0}^{\infty} \frac{A_n(\mathbf{x})}{(\sqrt{-i\omega})^n}. \tag{A10}$$

In this representation the first few terms of the series are the largest in magnitude and may be used to approximate the solution. The approach is similar to approximations used for ray methods in elasto-dynamics (Aki and Richards 1980). As pointed out by Virieux et al. (1994), if we expand the solution in inverse powers of $\sqrt{\omega}$, in the absence of any heterogeneity, our solution will reduce to the the solution of the diffusion equationin a homogeneous medium. Note that we can scale the frequency by a reference value ω_0 in order to ensure the scaled frequency ω/ω_0 is sufficiently small in magnitude.

An asymptotic solution for volume change follows if we substitude the series representation of $\hat{V}(\mathbf{x},\omega)$, expression (A10), into equation (A9) and apply the differential operators to each term in the series. For example, consider the gradient operator applied to expression (A10), which results in

$$\nabla \hat{V}(\mathbf{x},\omega) = e^{-\sqrt{-i\omega}\sigma(\mathbf{x})} \sum_{n=0}^{\infty} \frac{\nabla A_n(\mathbf{x})}{(\sqrt{-i\omega})^n} \tag{A11}$$

$$-\sqrt{-i\omega} \nabla \sigma(\mathbf{x}) e^{-\sqrt{-i\omega}\sigma(\mathbf{x})} \sum_{n=0}^{\infty} \frac{A_n(\mathbf{x})}{(\sqrt{-i\omega})^n}$$

and similarly for $\nabla \cdot \nabla V(\mathbf{x},\omega)$

$$\nabla \cdot \nabla \hat{V}(\mathbf{x},\omega) = e^{-\sqrt{-i\omega}\sigma(\mathbf{x})} \sum_{n=0}^{\infty} \frac{\nabla \cdot \nabla A_n(\mathbf{x})}{(\sqrt{-i\omega})^n}$$

$$-2\sqrt{-i\omega} e^{-\sqrt{-i\omega}\sigma} \sum_{n=0}^{\infty} \frac{\nabla \sigma \cdot \nabla A_n}{(\sqrt{-i\omega})^n}$$

$$-\sqrt{-i\omega} \nabla \cdot \nabla \sigma e^{-\sqrt{-i\omega}\sigma} \sum_{n=0}^{\infty} \frac{A_n}{(\sqrt{-i\omega})^n}$$

$$-i\omega \nabla \sigma \cdot \nabla \sigma e^{-\sqrt{-i\omega}\sigma} \sum_{n=0}^{\infty} \frac{A_n}{(\sqrt{-i\omega})^n}. \tag{A12}$$

The expressions (A11) and (A12) are composed of an infinite number of terms, each containing a factor that is a power of $1/\sqrt{\omega}$. Because we are assuming that ω, or it's scaled counter-part, is large, we are interested in terms of lowest order in $1/\sqrt{\omega}$. As found in Vasco et al. (2000) for the pressure equation, the lowest order terms are those of order -2:

$$(1/\sqrt{-i\omega})^{-2} = (\sqrt{-i\omega})^2 = i\omega. \tag{A13}$$

Collecting terms of order $i\omega$ gives

$$\nabla\sigma \cdot \nabla\sigma - \frac{C_e}{K} = 0, \tag{A14}$$

which is the eikonal equation governing the spatial variation of the phase. It is notable that the phase only depends upon the fluid diffusivity, which we denote by

$$\kappa = \frac{C_e}{K}, \tag{A15}$$

and is independent of the local geomechanical properties of the reservoir $\Pi(\mathbf{x})$. However, this does make physical sense because, due to the linearity inherent in elastic deformation, the peak rate of volume change shown occur at the same time as the peak rate of pressure change.

APPENDIX B: AN APPROXIMATE COVARIANCE MATRIX FOR THE LEAST SQUARES SOLUTION SUBJECT TO INEQUALITY CONSTRAINTS

In Appendix B we provide an overview of the approximation of the covariance matrix for the least squares solution of a problem containing inequality constraints, first presented by Liew (1976a, 1976b). The least squares solution of equation (1) is equivalent to a quadratic programming problem (Judge and Takayama 1966), in which one minimizes the quadratic function

$$\min \left\{ (\mathbf{u} - \boldsymbol{\Upsilon}\mathbf{v})^T \cdot (\mathbf{u} - \boldsymbol{\Upsilon}\mathbf{v}) \right\} \qquad (B1)$$

subject to linear inequality constraints

$$A\mathbf{v} \geq \mathbf{0}.$$

In equation (1) we have a simple requirement that the volume changes are negative resulting in: $\mathbf{A} = -\mathbf{I}$. The dual function of the primal problem (B1) provides the following relationship

$$-\mathbf{I}\boldsymbol{\Lambda} + \boldsymbol{\Upsilon}^T\mathbf{u} = (\boldsymbol{\Upsilon}^T\boldsymbol{\Upsilon})\mathbf{v} \qquad (B2)$$

(Dorn 1961, Hadley 1964). Equation (B1) can be solved using either the Lemke or Dantzig-Cottle algorithm (Cottle and Dantzig 1974) which requires the solution of

$$\left[\begin{array}{cc} \mathbf{I} & -\mathbf{W} \end{array} \right] \left[\begin{array}{c} \mathbf{y} \\ \boldsymbol{\Lambda} \end{array} \right] = \hat{\mathbf{v}} \qquad (B3)$$

subject to

$$\mathbf{y}^T\boldsymbol{\Lambda} = \mathbf{0}$$

$$\mathbf{y} \geq \mathbf{0}$$

$$\boldsymbol{\Lambda} \geq \mathbf{0}$$

where $\mathbf{W} = (\boldsymbol{\Upsilon}^T\boldsymbol{\Upsilon})^{-1}$ and $\hat{\mathbf{v}} = \boldsymbol{\Upsilon}^{\dagger}\mathbf{u}$ is the solution of the unconstrained problem given in terms of the generalized inverse $\boldsymbol{\Upsilon}^{\dagger}$. The vector $\boldsymbol{\Lambda}$ is a vector of Lagrange multipliers associated with the inequality constraints. We indicate the solution of equation (B3) by the starred variables $\mathbf{y}^*$ and $\boldsymbol{\Lambda}^*$. Substituting $\boldsymbol{\Lambda}^*$ into equation (B2) and multiplying both sides by $\mathbf{W} = (\boldsymbol{\Upsilon}^T\boldsymbol{\Upsilon})^{-1}$ we get an expression for $\mathbf{v}$ in terms of $\hat{\mathbf{v}}$

$$\mathbf{v} = \hat{\mathbf{v}} - (\boldsymbol{\Upsilon}^T\boldsymbol{\Upsilon})^{-1}\boldsymbol{\Lambda}^*. \qquad (B4)$$

Once we have the Lagrange multiplier vector, $\boldsymbol{\Lambda}$, we can rewrite (B3)

$$\left[\begin{array}{cc} \mathbf{I}_b & -\mathbf{W}_b \end{array} \right] \mathbf{b} + \left[\begin{array}{cc} \mathbf{I}_{nb} & -\mathbf{W}_{nb} \end{array} \right] \mathbf{n} = \hat{\mathbf{v}} \qquad (B5)$$

where

$$\mathbf{b} = \left[\begin{array}{c} \mathbf{y}_b \\ \boldsymbol{\Lambda}_b \end{array} \right]$$

is the vector of the basic variables and

$$\mathbf{n} = \left[\begin{array}{c} \mathbf{y}_{nb} \\ \boldsymbol{\Lambda}_{nb} \end{array} \right]$$

is the vector of the nonbasic variables containing only null elements. Using this decomposition and the fact that the second term on the left of equation (B5) vanishes, we can write

$$\left[\begin{array}{c} \mathbf{y}_b \\ \boldsymbol{\Lambda}_b \end{array} \right] = \left[\begin{array}{cc} \mathbf{I}_b & -\mathbf{W}_b \end{array} \right]^{-1} \hat{\mathbf{v}} = \left[\begin{array}{c} \mathbf{M}_1 \\ \mathbf{M}_2 \end{array} \right] \hat{\mathbf{v}}, \qquad (B6)$$

where the matrix on the right

$$\mathbf{M} = \left[\begin{array}{c} \mathbf{M}_1 \\ \mathbf{M}_2 \end{array} \right]$$

is just a decomposition of $\left[\begin{array}{cc} \mathbf{I}_b & -\mathbf{W}_b \end{array} \right]^{-1}$ into a matrix $\mathbf{M}$ with rows $\mathbf{M}_1$ associated with $\mathbf{y}_b$ and rows $\mathbf{M}_2$ associated with $\boldsymbol{\Lambda}_b$. From the lower set of equations in (B6) we arrive at an expression for the Lagrange multipliers associated with the basic variables in terms of the solution vector $\hat{\mathbf{v}}$

$$\boldsymbol{\Lambda}_b = \mathbf{M}_2\hat{\mathbf{v}}. \qquad (B7)$$

Because only the basic elements of $\boldsymbol{\Lambda}^*$ are nonzero we may write $\boldsymbol{\Lambda}^*$ in the form

$$\boldsymbol{\Lambda}^* = \left[\begin{array}{c} \mathbf{0} \\ \boldsymbol{\Lambda}_b \end{array} \right].$$

We can write $\boldsymbol{\Lambda}^*$ in an expanded, partitioned form

$$\boldsymbol{\Lambda}^* = \left[\begin{array}{cc} \mathbf{I}_1 & \mathbf{I}_2 \end{array} \right] \left[\begin{array}{c} \mathbf{0} \\ \boldsymbol{\Lambda}_b \end{array} \right] = \mathbf{I}_2\boldsymbol{\Lambda}_b \qquad (B8)$$

where $\mathbf{I}_2$ are the left-most b columns of the identity matrix. Combining the expressions (B4), (B7), and (B8) we can write $\mathbf{v}$ in terms of $\hat{\mathbf{v}}$

$$\mathbf{v} = [\mathbf{I} - (\boldsymbol{\Upsilon}^T\boldsymbol{\Upsilon})^{-1}\mathbf{I}_2\mathbf{M}_2]\hat{\mathbf{v}} \qquad (B9)$$

or

$$\mathbf{v} = \mathbf{Q}\hat{\mathbf{v}} \qquad (B10)$$

where $\mathbf{Q}$ is the matrix

$$\mathbf{Q} = [\mathbf{I} - (\boldsymbol{\Upsilon}^T\boldsymbol{\Upsilon})^{-1}\mathbf{I}_2\mathbf{M}_2] \qquad (B11)$$

(Liew 1976a, Liew 1976b). The apparent linear relationship between $\mathbf{v}$ and $\hat{\mathbf{v}}$ in equation (B10) suggests that we can map the covariance matrix of the unconstrained problem $\mathbf{C}_{vv}$ into the covariance matrix of the constrained problem $\mathbf{C}_{v_cv_c}$,

$$\mathbf{C}_{v_cv_c} = \mathbf{Q}\mathbf{C}_{vv}\mathbf{Q}^T. \qquad (B12)$$

However, because $\mathbf{I}_2$ and $\mathbf{M}_2$ depend upon the final solution, specifically upon the partitioning of the basic and non-basic variables, the matrix $\mathbf{Q}$ is actually dependent upon the data $\mathbf{u}$ and the covariance matrix is only an approximation.

REFERENCES

Aki, K., and P. G. Richards, 1980, Quantitative seismology: Freeman and Sons.

Al-Hussainy, R., Ramey, Jr., H. J., and Crawford, P. B., 1966, The flow of real gases through porous media, Journal of Petroleum Technology, **18**, 624-636.

Amelung, F., D. L. Galloway, J. W. Bell, H. A. Zebker, and R. J. Laczniak, 1999, Sensing the ups and downs of Las Vegas-InSAR reveals structural control of land subsidence and aquifer-system deformation: Geology, **27** , 483-486.

Aronofsky, J. S., and Jenkins, R., 1954, A simplified analysis of unsteady radial gas flow, Transactions of the American Institute of Mechanical Engineering, **201** , 149-192.

Arts, R., O. Eikan, A. Chadwick, P. Zweigel, L. van der Meer, and B. Zinszner, 2004, Monitoring of CO_2 injected at Sleipner using time-lapse seismic data: Energy **29**, 1383-1392.

Barrett, R., M. Berry, T. F. Chan, et al., 1994, Templates for the Solution of Linear Systems: Building Blocks for Iterative Methods, SIAM, Philadelphia.

Bracewell, R. N., 1978, The Fourier Transform and It's Applications: McGraw-Hill, New York.

Bruno, M. S., and R. A. Bilak, 1994, Cost-effective monitoring of injected steam migration using surface deformation analysis: Society of Petroleum Engineers Western Regional Meeting., **27888** , 397-412.

Castle, R. O., R. F. Yerkes, and F. S. Riley, 1969, A linear relationship between liquid production and oil-related subsidence: in Tison, L. J., (Ed.), Land subsidence, **1** , International Association of Scientific Hydrology Publications, (88), 597-604.

Cohen, J. K., and R. M. Lewis, 1967, A ray method for the asymptotic solution of the diffusion equation, Journal of the Institute of Mathematics and its Applications, **3**, 266-290.

Coleman, T.F. and Y. Li, 1996, A Reflective Newton Method for Minimizing a Quadratic Function Subject to Bounds on Some of the Variables, SIAM Journal on Optimization, Vol. 6, Number 4, pp. 1040-1058.

Courant, R., and D. Hilbert, 1962, Methods of Mathematical Physics: Interscience.

Cottle, R.W., and Dantzig, G.B., 1974, Complementary Pivot of Mathematical Programming: J. Abadie ed. Nonlinear Programming, Amsterdam: North Holland Publishing Co., 55-73

Crank, J., 1975, The Mathematics of Diffusion: Oxford University Press, London.

de Marsily, G., 1986, Quantitative hydrogeology: Academic Press.

Dorn, W.S., 1961, Self-Dual Quadratic Programs: Journal of Society for Industrial and Applied Mathematics, **9**, 51-54.

Du, J., and J. E. Olson, 2001, A poroelastic reservoir model for predicting subsidence and mapping subsurface pressure fronts: Journal of Petroleum Science and Engineering, **30** , 181-197.

Du, J., S. J. Brissenden, P. McGillivray, S. Bourne, P. Hofstra, E. J. Davis, W. H. Roadarmel, S. L. Wolhart, S. Marsic, R. Gusek, and C. A. Wright, 2005, Mapping reservoir volume changes during cyclic steam stimulation using tiltmeter based surface deformation measurements, 2005 Society of Petroleum Engineers International Thermal Operations and Heavy Oil Symposium, **CHOA 97848**, Calgary, Alberta, Canada, 1-3 November 2005.

Dussealt, M. B., R. A. Bilak, and L. Rothenburg, 1993, Inversion of surface displacements to monitor in-situ processes: International Journal of Rock Mechanics and Mining Science, **30** , 1219-1222.

Fielding, E. J., R. G. Blom, and R. M. Goldstein, 1998, Rapid subsidence over oil fields measured by SAR interferometry: Geophysical Research Letters, **25**, 3215-3218.

Ferretti, A., C. Prati, and F. Rocca, 2000, Nonlinear subsidence rate estimation using permanent scatterers in differential SAR interferometry: Institute of Electrical and Electronics Engineers Transactions on Geoscience and Remote Sensing, **38** , 2202-2212.

Ferretti, A., Prati, C, and Rocca, F., 2001, Permanent scatterers in SAR interferometry: Institute of Electrical and Electronics Engineers Transactions on Geoscience and Remote Sensing, **39** , 8-20.

Geertsma, J., 1973, Land subsidence above compacting oil and gas reservoirs, Journal of Petroleum Technology, 734-744.

Gill, P.E., W. Murray, and M.H. Wright, 1981, Practical Optimization, Academic Press, London, UK.

Hadley, G., 1962, Linear Programming: Addison-Wesley.

Hadley, G., 1964, Nonlinear and Dynamic Programming: Addison-Wesley.

Hodgson, N., C. MacBeth, L. Duranti, J. Rickett, and K. Nihei, 2007, Inverting for reservoir pressure change using time-lapse time strain: Application to tthe Genesis Field, Gulf of Mexico: The Leading Edge, **26** , 649-652. Humphreys and Clayton, 1988

Humphreys. E. , Clayton. R.W. and Hager. B.H., 1988, Adaptation of back projection tomography to seismic travel time problems: Journal of Geophysical Research, **93** , 1073-1085.

Johnson, N. L., and S. Kotz, 1970, Continuous Univariate Distributions - 1: John Wiley and Sons.

Judge, G. G., and T. Takayama, 1966, Inequality restrictions in regression analysis: The Journal of the American Statistical Association, **61** , 166-181.

Liew, C.K., 1976a, A Two-Stage Least-Squares Estimation with Inequality Restrictions on Parameters: The Review of Economics and Statistics, **58** , 234-238.

Liew, C.K., 1976b, Inequality Constrained Least-Squares Estimation: The Journal of the American Statistical Association, **71** , 746-751.

Liu, Y., and Helm, D. C., 2008, Inverse procedure for calibrating parameters that control land subsidence caused by subsurface fluid withdrawl: 1. Methods: Water Resources Research, **44**, 1-15.

Menke, W., 1984. Geophysical Data Analysis: Discrete Inverse Theory: Academic Press.

Mossop, A., and P. Segall, 1999, Volume strain within the Geysers geothermal field: Journal of Geophysical Research, **104** , 29113-29131.

Muskat, M., 1946, Flow of Homogeneous Fluids Through Porous Media: J. W. Edwards, Ann Arbor, MI.

Parker, R. L., 1994, Geophysical inverse theory: Princeton University Press.

Press, F., 1968, Density distribution in the Earth, Science, **160**, 1218-1221.

Rice, J. R., and M. P. Cleary, 1976, Some basic stress diffusion solutions for fluid-saturated elastic porous media with compressible constituents: Reviews of Geophysics and Space Physics, **14**, 227-241.

Rickett, J., L. Duranti, T. Hudson, B. Regel, and N. Hodgson, 2007, 4-D time strain and the seismic signature of geomechanical compaction at Genesis: The Leading Edge, **26** , 644-647.

Roste, T., A. Stovas, and M. Landro, 2006, Estimation of layer thickness and velocity changes using 4D prestack seismic data: Geophysics, **71**, S219-S234.

Schmidt, D. A., and R. Burgmann, 2003, Time-dependent land uplift and subsidence in the Santa Clara valley, California, from a large interferometric synthetic aperture radar data set: Journal of Geophysical Research, **108**, doi:10.1029/20002JB002267,4-1/4-13.

Segall, P., 1985, Stress and subsidence resulting from subsurface fluid withdrawal in the epicentral region of the 1983 Coalinga earthquake: Journal of Geophysical Research, **90**, 6801-6816.

Stancliffe, R. P. W., and M. W. A. van der Kooij, 2001, The use of satellite-based radar interferometry to monitor production activity at the Cold Lake heavy oil field, Alberta, Canada: American Association of Petroleum Geologists Bulletin, **85**, 781-793.

Staples, R., J. Ita, R. Burrell, and R. Nash, 2007, Monitoring pressure depletion and improving geomechanical models of the Shearwater Field using 4D seismic: The Leading Edge, **26** , 636-642.

Tarantola, A., 2005, Inverse Problem Theory and Model Parameter Estimation: SIAM.

Tura, A., T. Barker, P. Cattermile, C. Collins, J. Davis, P. Hatchell, K. Koster, P. Schutjens, and P. Willis, 2005, Monitoring primary depletion reservoirs using amplitudes and time shifts from high-repeat seismic surveys: The Leading Edge, **24**, 1214-1221.

Vasco, D. W., L. R. Johnson, and N. Goldstein, 1988, Using surface deformation and strain observations to determine deformation at depth, with an application to Long Valley Caldera, California: Journal of Geophysical Research, **93** , 3232-3242.

Vasco, D. W., R. B. Smith, and C. L. Taylor, 1990, Inversion for sources of crustal deformation and gravity change at the Yellowstone caldera, Journal of Geophysical Research, **95**, 19839-19856.

Vasco, D. W., K. Karasaki, and C. Doughty, 2000a, Using surface deformation to image reservoir dynamics: Geophysics, 65 , 132-147.

Vasco, D. W., K. Karasaki, and H. Keers, 2000b, Estimation of reservoir properties using transient pressure data: An asymptotic approach: Water Resources Research, **36**, 3447-3465.

Vasco, D. W., K. Karasaki, and K. Kishida, 2001. A coupled inversion of pressure and surface displacement: Water Resources Research, **37**, 3071-3089.

Vasco, D. W., and A. Ferretti, 2005, On the use of quasi-static deformation to understand reservoir fluid flow: Geophysics, **70**, O13-O27.

Vasco, D. W., A. Ferretti, and Novali, 2008, Estimating permeability from quasi-static deformation: Temporal variations and arrival-time inversion, Geophysics, **73**, O37-O52.

Vasco, D. W., A. Rucci, A. Ferretti, F. Novali, R. C. Bissell, P. S. Ringrose, A. S. Mathieson, and I. W. Wright,

2010, Satellite-based measurements of surface deformation reveal fluid flow associated with the geological storage of carbon dioxide, Geophysical Research Letters, **37**, L03303, doi:10.1029/2009GL041544, 1-5.

Virieux, J., C. Flores-Luna, and D. Gibert, 1994, Asymptotic theory for diffusive electromagnetic imaging: Geophysical Journal International, **119**, 857-868.

Wang, R., and H.-J., Kuempel, 2003, Poroelasticity: Efficient modeling of strongly coupled, slow deformation processes in a multilayered half-space: Geophysics, **68**, 705-717.

White, D. J., G. Burrowes, T. Davis, Z. Hajnal, K. Hirsche, I. Hutcheon, E. Majer, B. Rostron, and S. Whittaker, 2004, Greenhouse gas sequestration in abandoned oil reservoirs: The International Energy Agency Weyburn pilot project: GSA Today **14**, 4-10.

FIGURE CAPTIONS

Figure 1 Range changes for four time intervals. The production wells surface traces are indicated by solid lines in the figure. Well KB−11 started the production on July 2004, well KB−12 on September 2004 and well KB−14 on May 2005.

Figure 2 Contour map indicating the depth, in kilometers, to the top of the reservoir. The depths are referenced to mean sea level.

Figure 3 Estimates of percentage volume change (normalized) from the unconstrained inversion of the range change observations (Figure 1).

Figure 4 Estimates of percentage volume change (normalized) from the an inversion of the range change observations (Figure 1) that incorporates inequality constraints.

Figure 5 Diagonal elements of the resolution matrix plotted in the corresponding grid block positions. These estimates were computed without inequality constraints.

Figure 6 Averaging kernels for four different locations in the reservoir model. These estimates were computed without inequality constraints.

Figure 7 Diagonal elements of the resolution matrix (normalized) computed with inequality constraints.

Figure 8 Averaging kernels (normalized) for four locations in the reservoir model, computed with inequality constraints.

Figure 9 Standard deviation (normalized) for the estimates of percentage volume change, computed without inequality constraints.

Figure 10 Standard deviation (normalized) for the estimates of percentage volume changes computed using the Monte Carlo approach for the inequality constrained least squares solution.

Figure 11 Sets of histograms displaying the variation in the solutions obtained using Monte Carlo simulation. (Left Panel) Unconstrained least squares estimates. (Right Panel) Least squares with inequality constraints.

Figure 12 Standard deviation (normalized) for the estimates of percentage volume change computed using the analytical approximation, equation (17), for the inequality constrained least squares solution.

Figure 13 Standard deviation (normalized) for the estimates of percentage volume change computed using equation (21) for the inequality constrained least squares solution.

Figure 14 A scatter plot comparing two estimates of the standard deviation in presence of inequality constraints. We plot estimates obtained using equation (17) against estimates obtained using equation (21).

Figure 15 Relative pressure change (normalized) from an inversion of the range change observations in which inequality constraints were included but not lateral variation in compressibility.

Figure 16 The arrival time of the transient pressure field for the region near well KB−11 inferred from the volume change estimates shown in Figure 4, including inequality constraint in the inversion.

Figure 17 Relative pressure change (normalized) from an inversion of the range change observations in which inequality constraints and lateral variation in compressibility were included.

Figure 18 The arrival time of the transient pressure field for the region near well KB−11, in case of inequality constraint, estimated from the relative pressure change estimates shown in Figure 17, where lateral variation in compressibility were considered in the inversion.

Figure 19 Trajectories calculated from the constrained estimates of diffusive travel times (Figure 18).

Figure 20 Logarithm of the permeability multipliers obtained from an inversion of the travel times in Figure 18, using the trajectories shown in Figure 19.

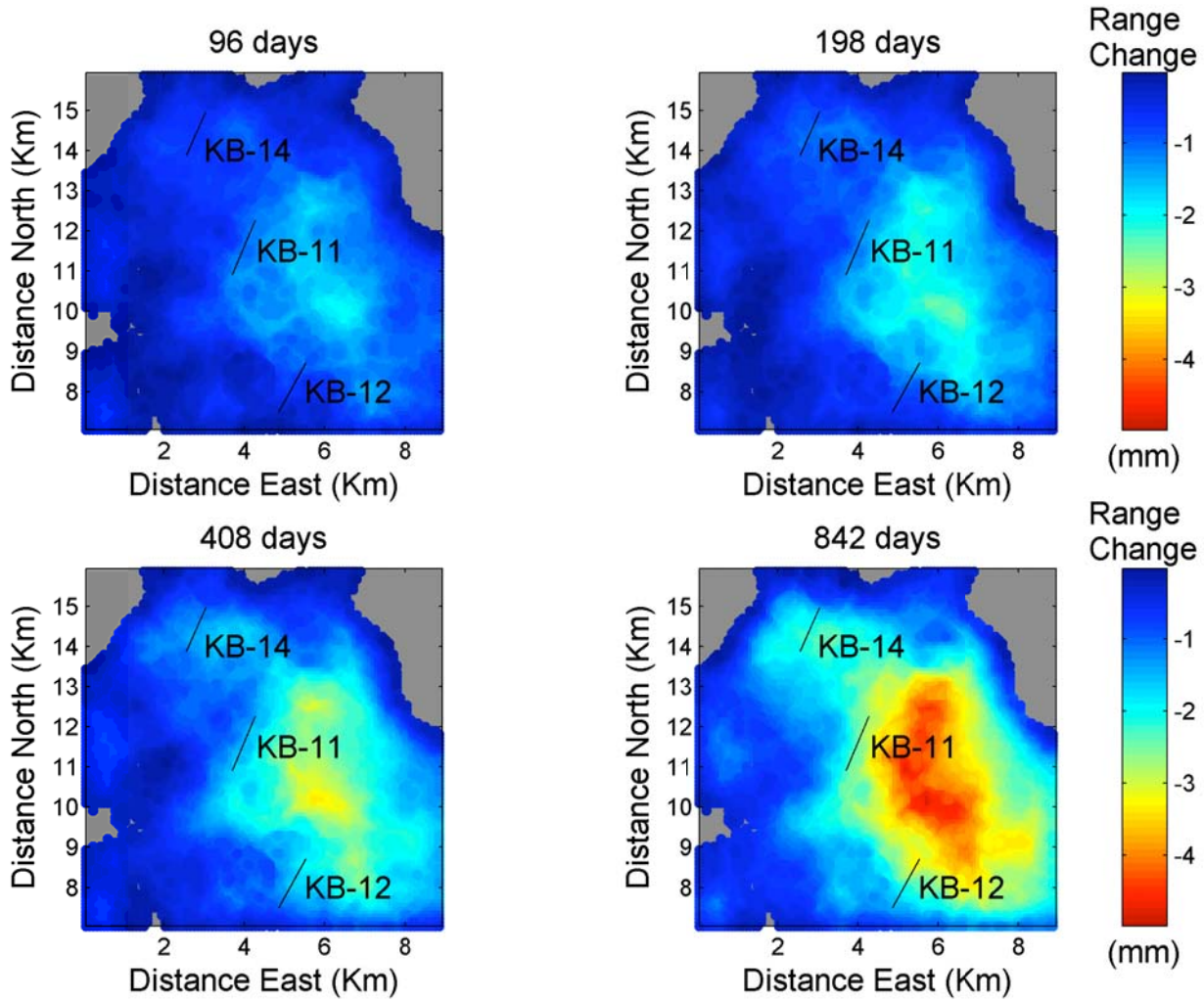
96 days
198 days
408 days
842 days
KB-14
KB-11
KB-12
Distance North (Km)
Distance East (Km)
Range Change
(mm)
-1
-2
-3
-4
2
4
6
8
9
10
11
12
13
14
15

Figure 1

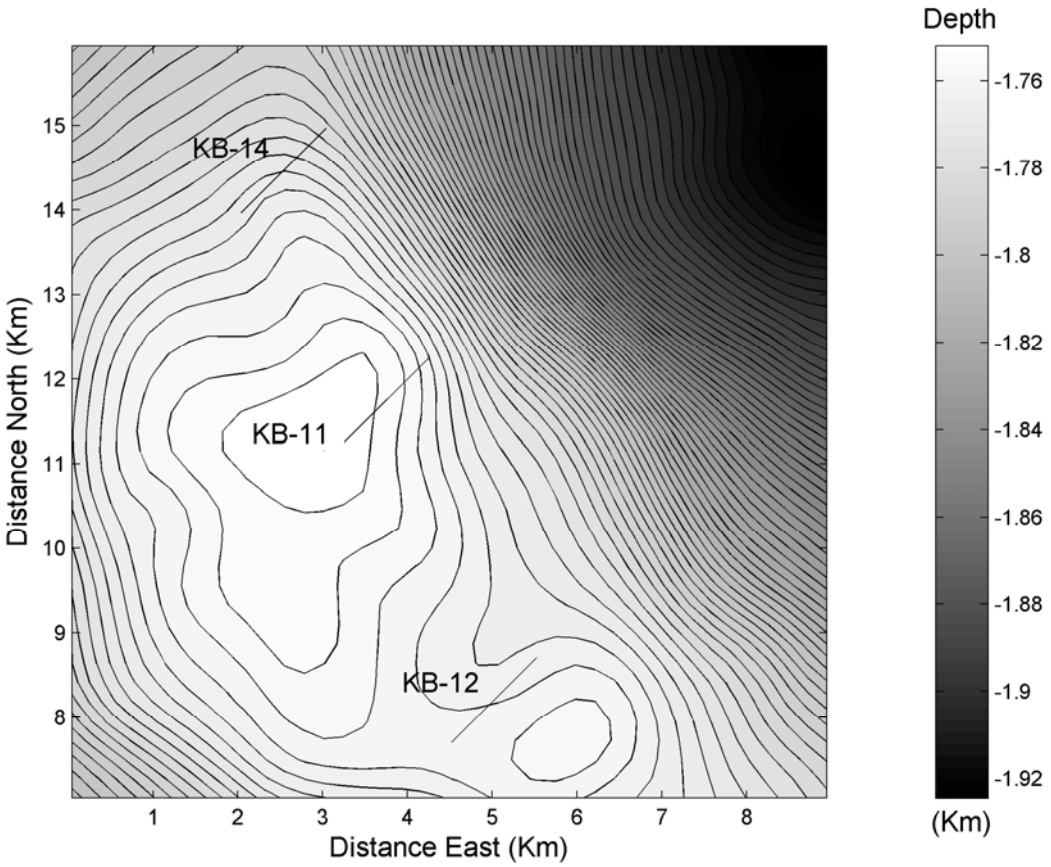
Depth
-1.76
-1.78
-1.8
-1.82
-1.84
-1.86
-1.88
-1.9
-1.92
(Km)
KB-14
KB-11
KB-12
Distance North (Km)
Distance East (Km)
15
14
13
12
11
10
9
8
1
2
3
4
5
6
7
8

Figure 2

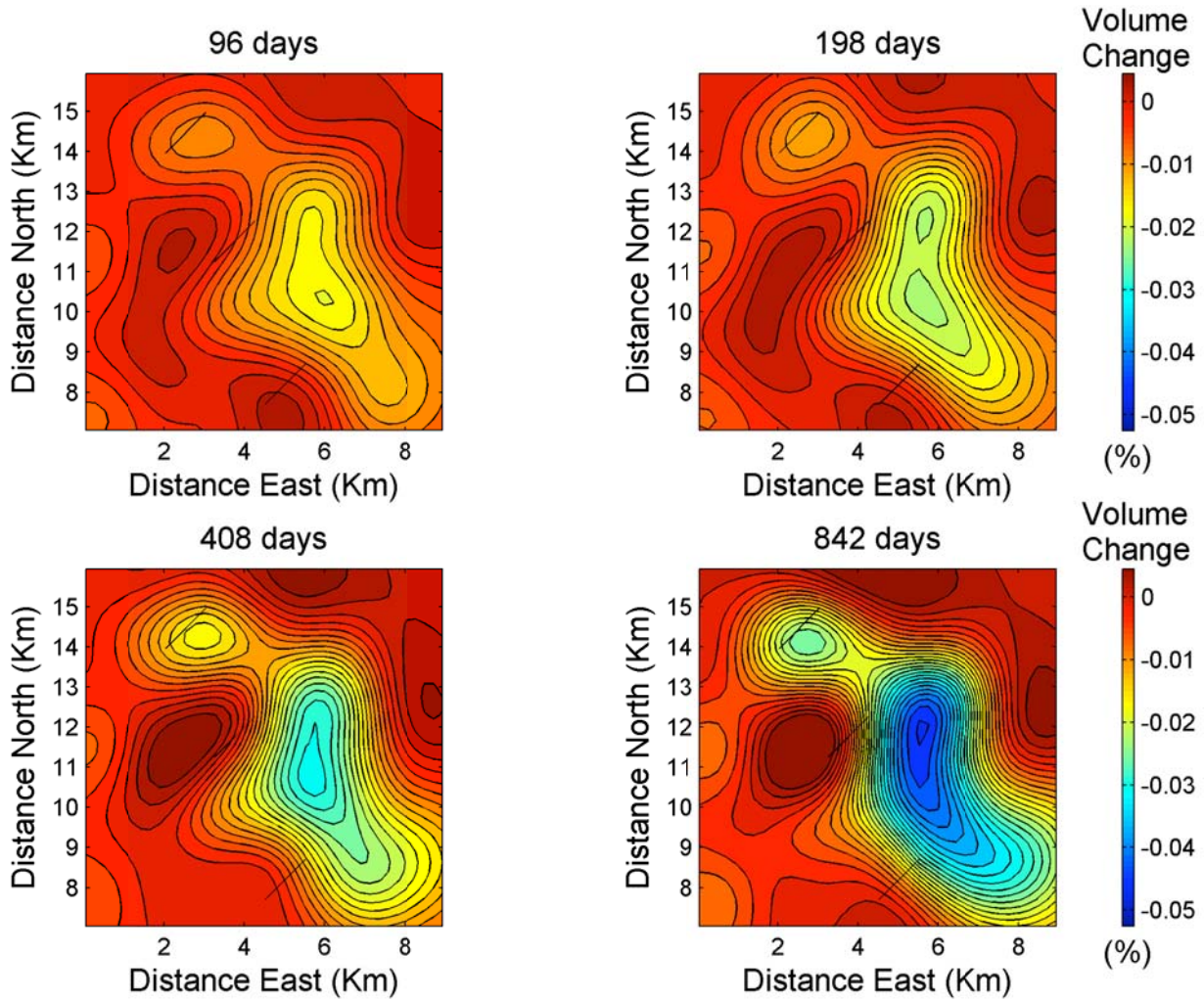
96 days
198 days
408 days
842 days
Distance North (Km)
Distance East (Km)
Volume Change
0
-0.01
-0.02
-0.03
-0.04
-0.05
(%)

Figure 3

96 days
198 days
408 days
842 days
Distance North (Km)
Distance East (Km)
Volume Change
-0.01
-0.02
-0.03
-0.04
-0.05
(%)

Figure 4

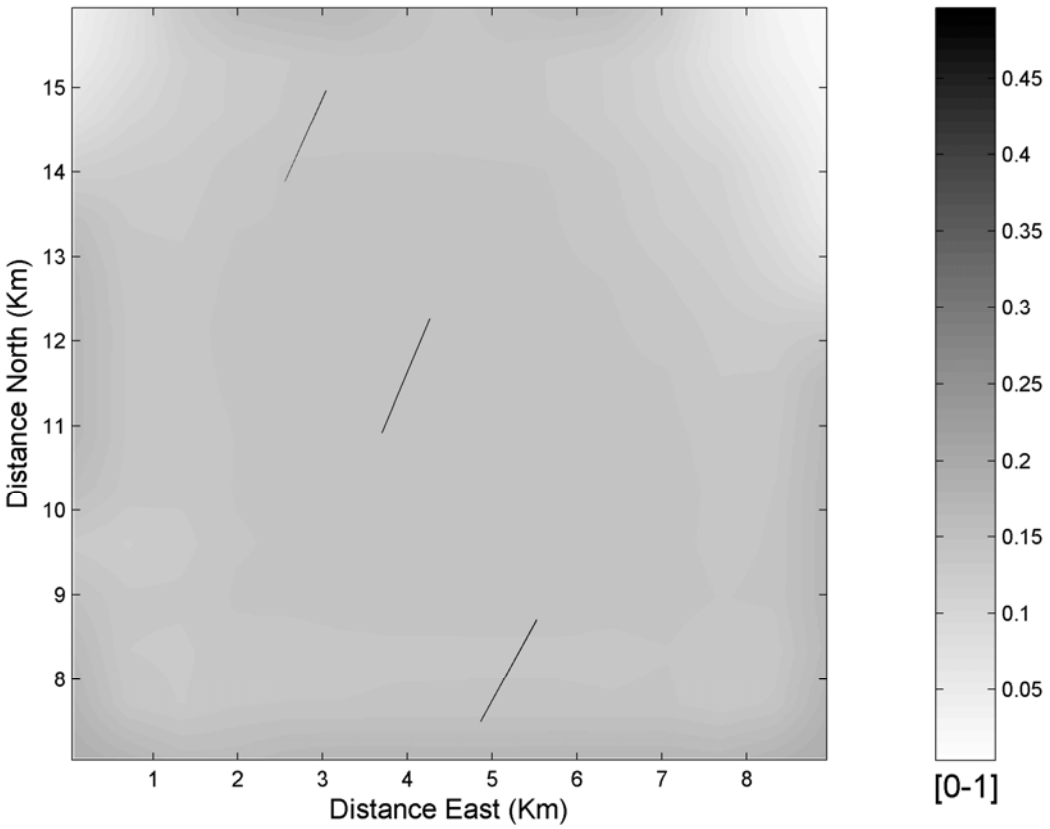
Distance North (Km)
15
14
13
12
11
10
9
8
1
2
3
4
5
6
7
8
Distance East (Km)
0.45
0.4
0.35
0.3
0.25
0.2
0.15
0.1
0.05
[0-1]

Figure 5

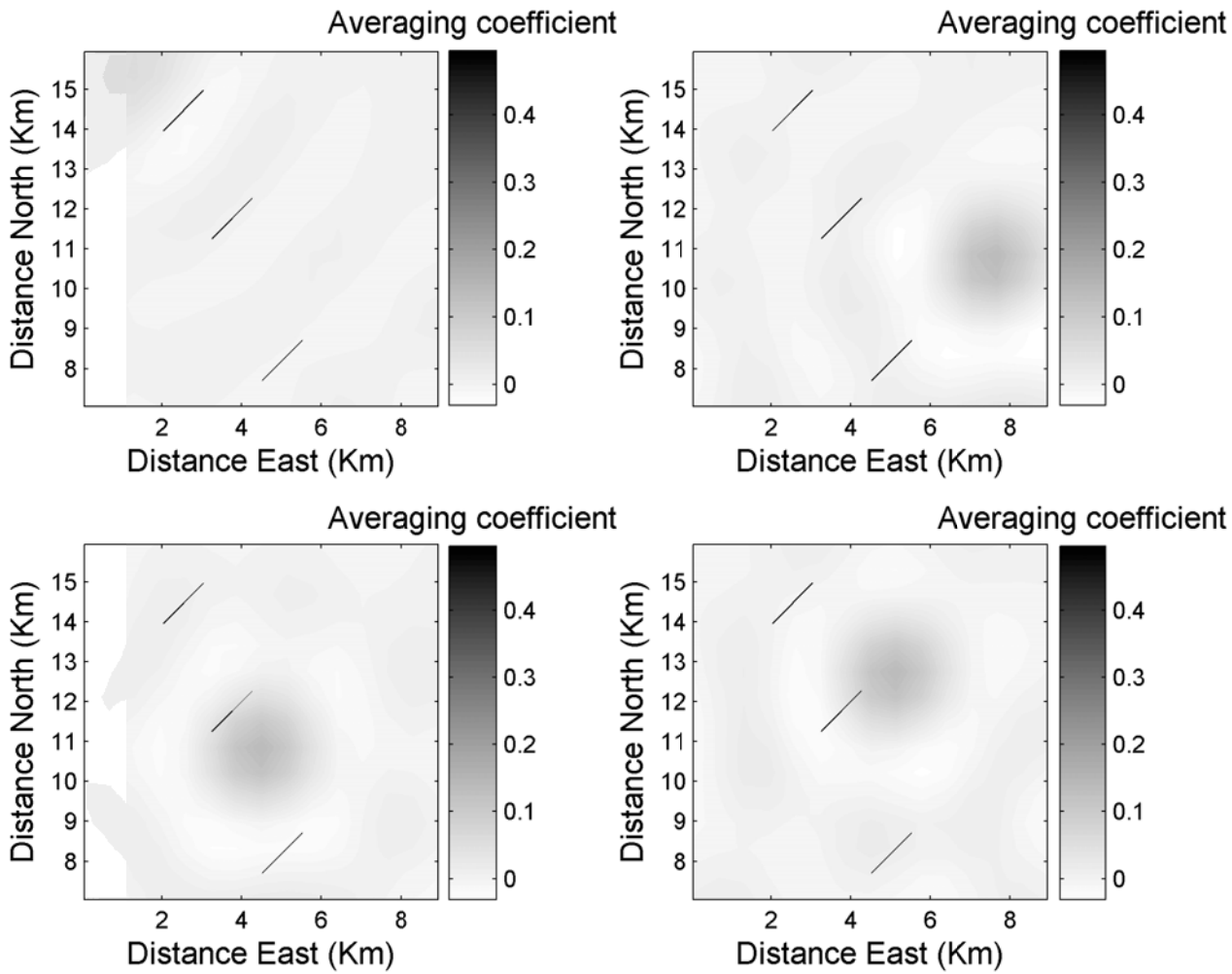
Averaging coefficient
Distance North (Km)
Distance East (Km)
Averaging coefficient
Distance North (Km)
Distance East (Km)
Averaging coefficient
Distance North (Km)
Distance East (Km)
Averaging coefficient
Distance North (Km)
Distance East (Km)

Figure 6

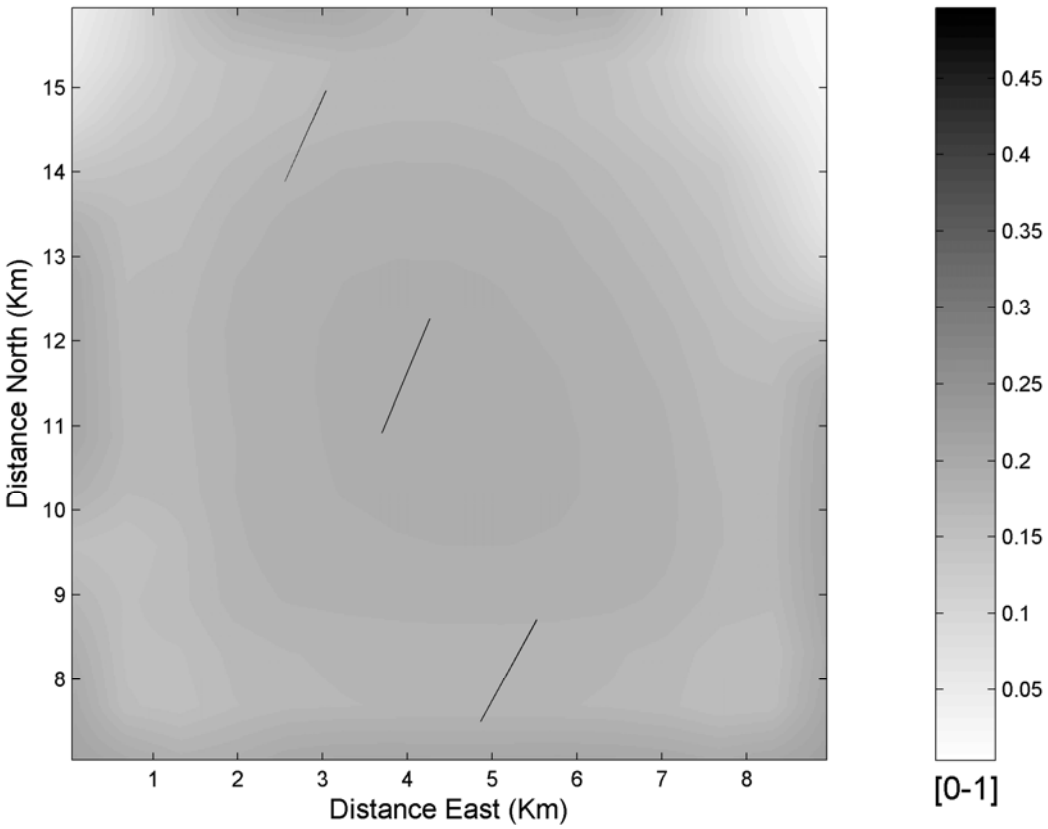
Distance North (Km)
15
14
13
12
11
10
9
8
1
2
3
4
5
6
7
8
Distance East (Km)
0.45
0.4
0.35
0.3
0.25
0.2
0.15
0.1
0.05
[0-1]

Figure 7

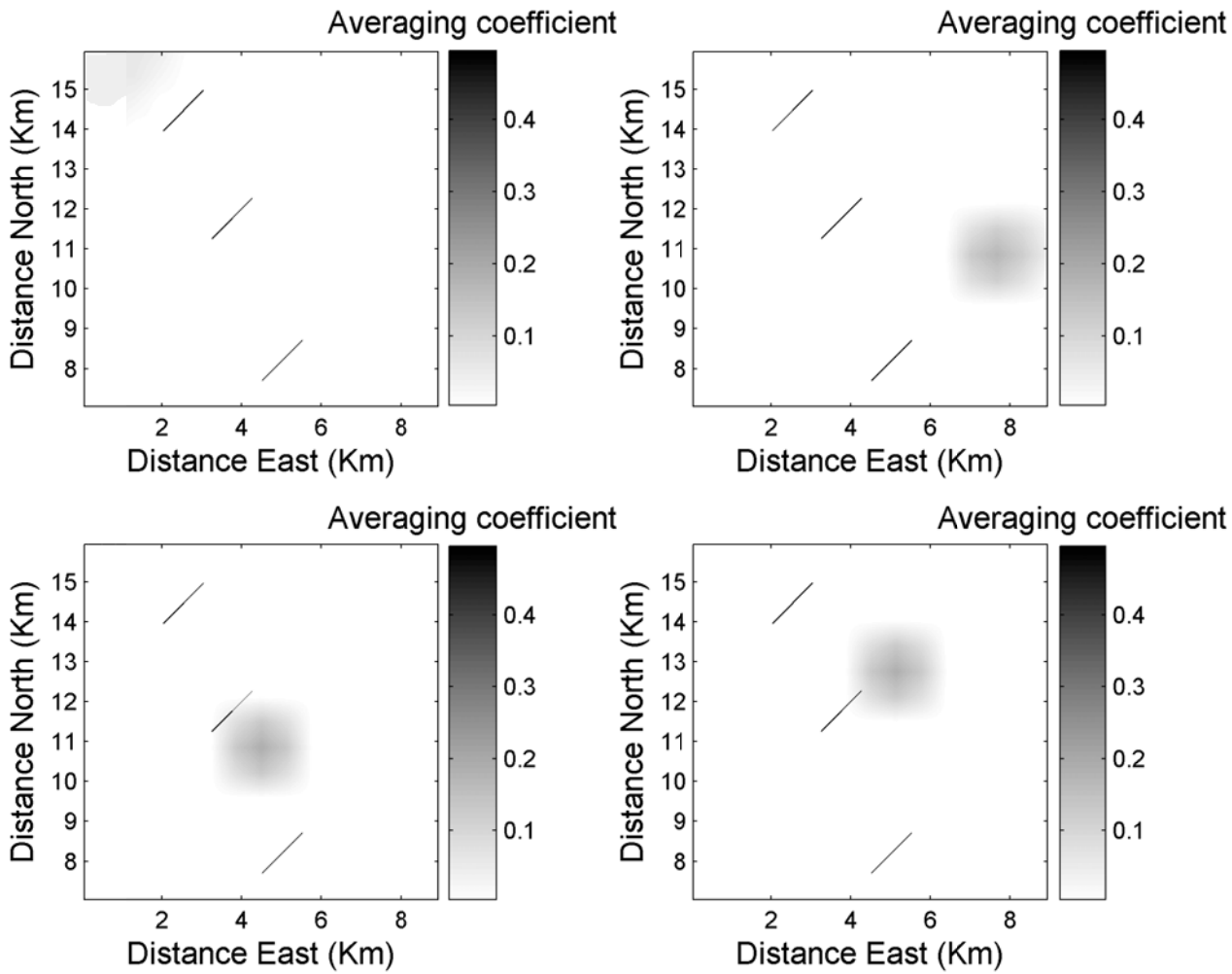
Averaging coefficient
Distance North (Km)
Distance East (Km)
Averaging coefficient
Distance North (Km)
Distance East (Km)
Averaging coefficient
Distance North (Km)
Distance East (Km)
Averaging coefficient
Distance North (Km)
Distance East (Km)

Figure 8

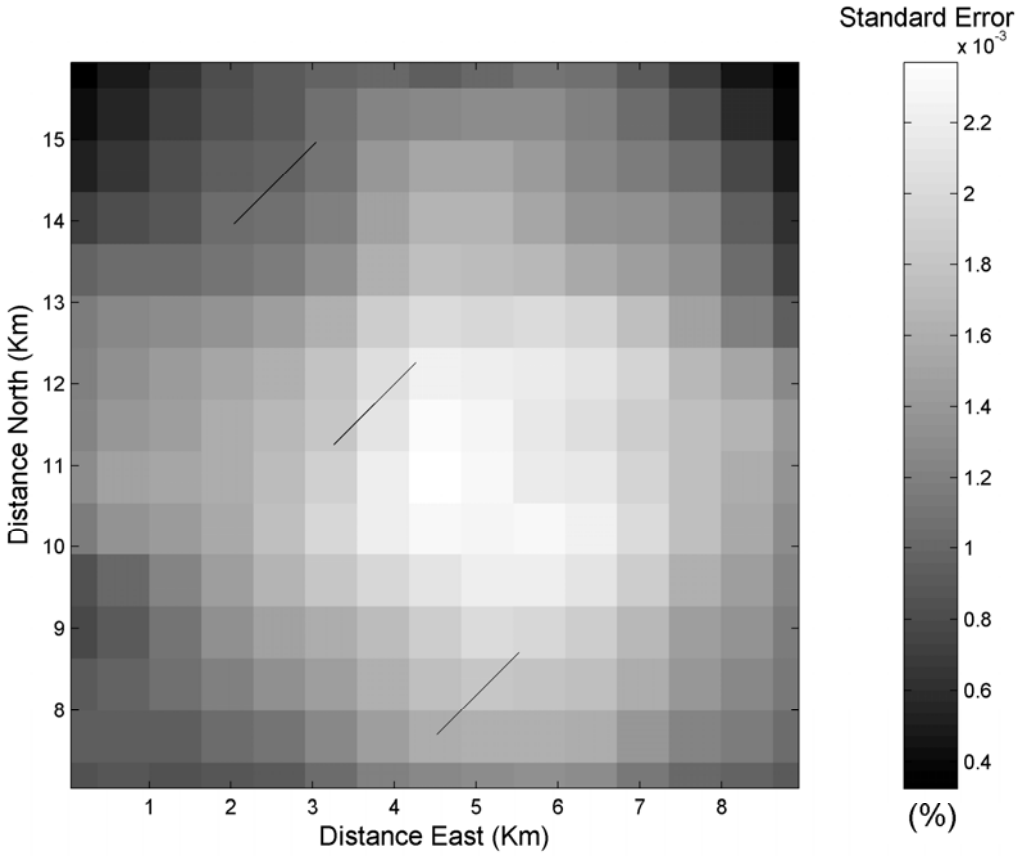
Standard Error
x 10^-3
2.2
2
1.8
1.6
1.4
1.2
1
0.8
0.6
0.4
(%)
Distance North (Km)
15
14
13
12
11
10
9
8
1
2
3
4
5
6
7
8
Distance East (Km)

Figure 9

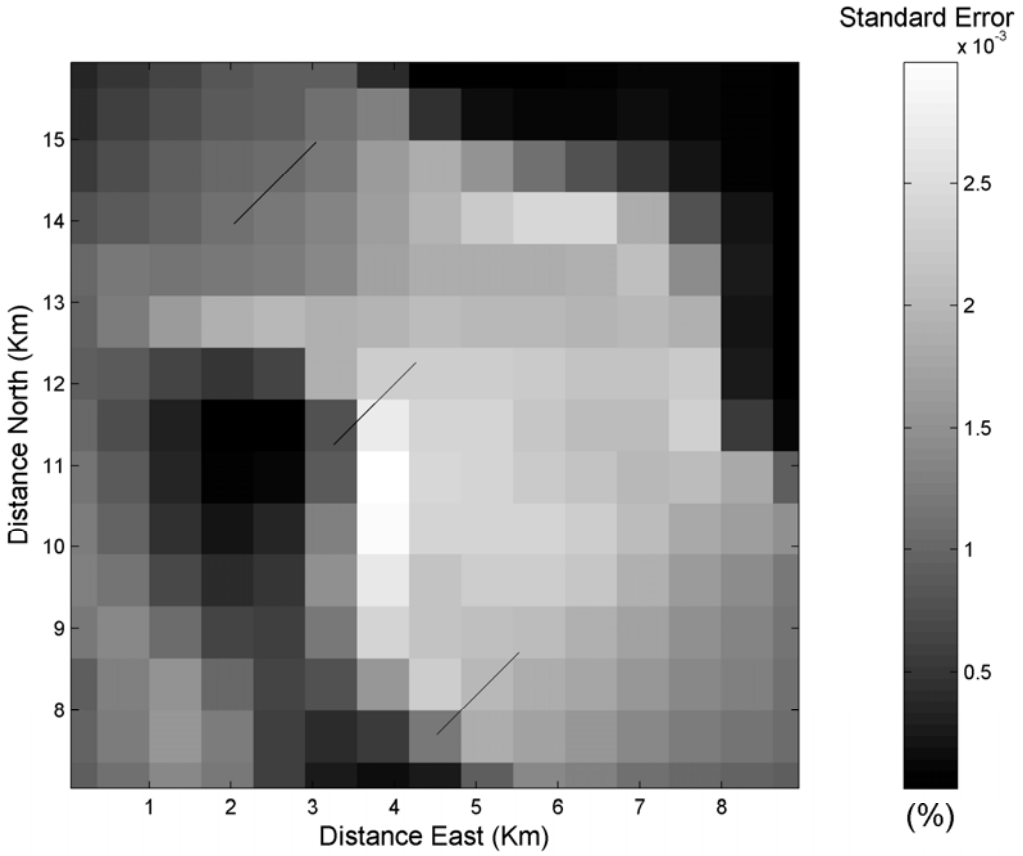
Standard Error
x 10^-3
2.5
2
1.5
1
0.5
(%)
Distance North (Km)
15
14
13
12
11
10
9
8
1
2
3
4
5
6
7
8
Distance East (Km)

Figure 10

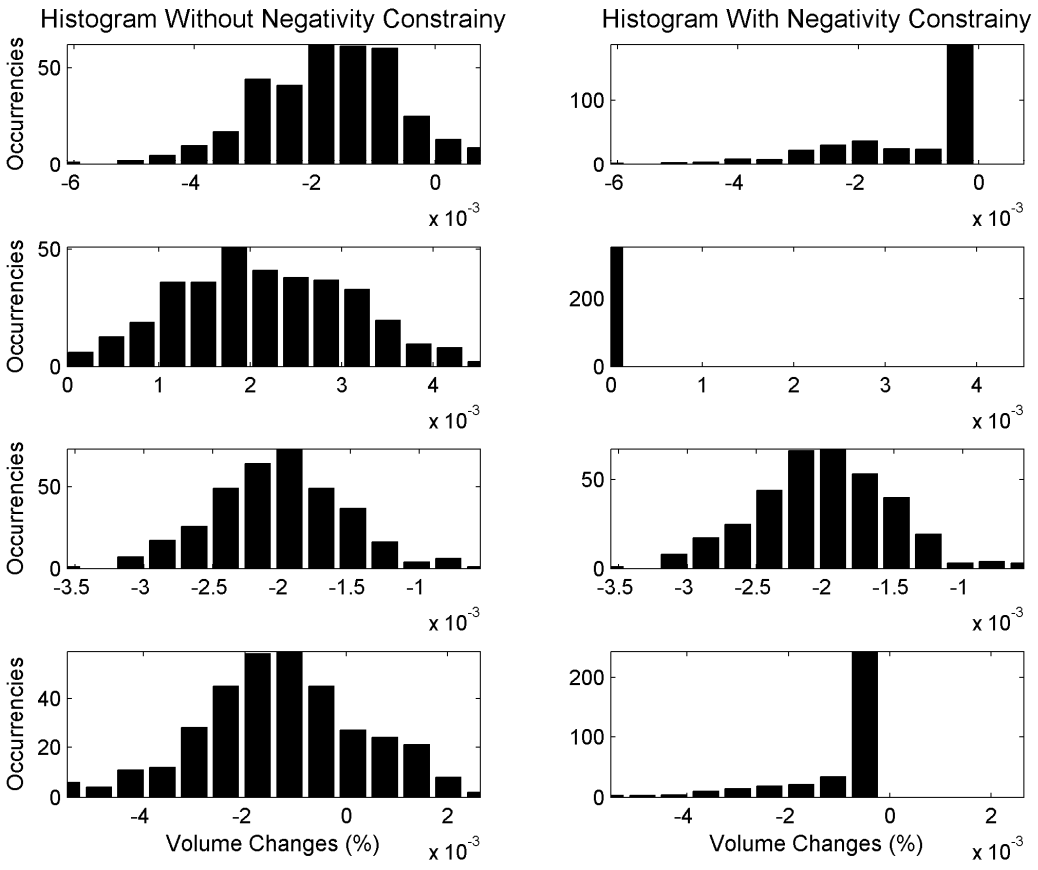
Histogram Without Negativity Constrainy
Histogram With Negativity Constrainy
Occurrencies
Volume Changes (%)
x 10^-3

Figure 11

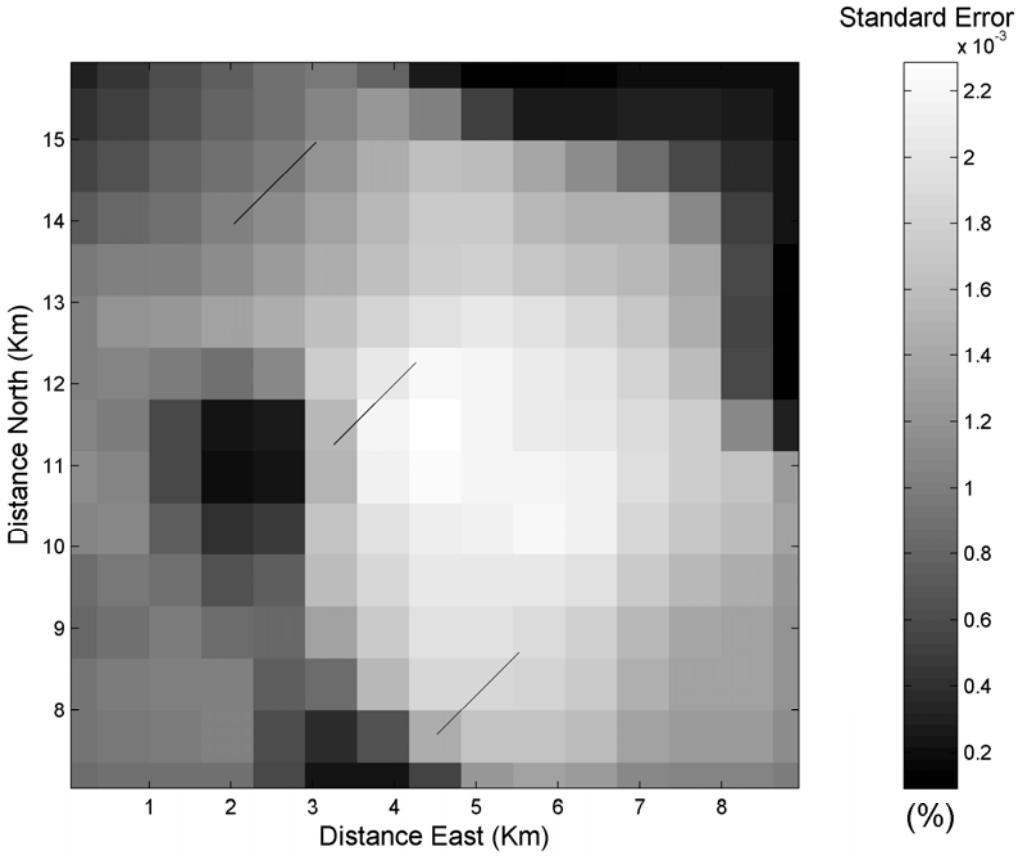
Standard Error
x 10^-3
2.2
2
1.8
1.6
1.4
1.2
1
0.8
0.6
0.4
0.2
(%)
Distance North (Km)
15
14
13
12
11
10
9
8
1
2
3
4
5
6
7
8
Distance East (Km)

Figure 12

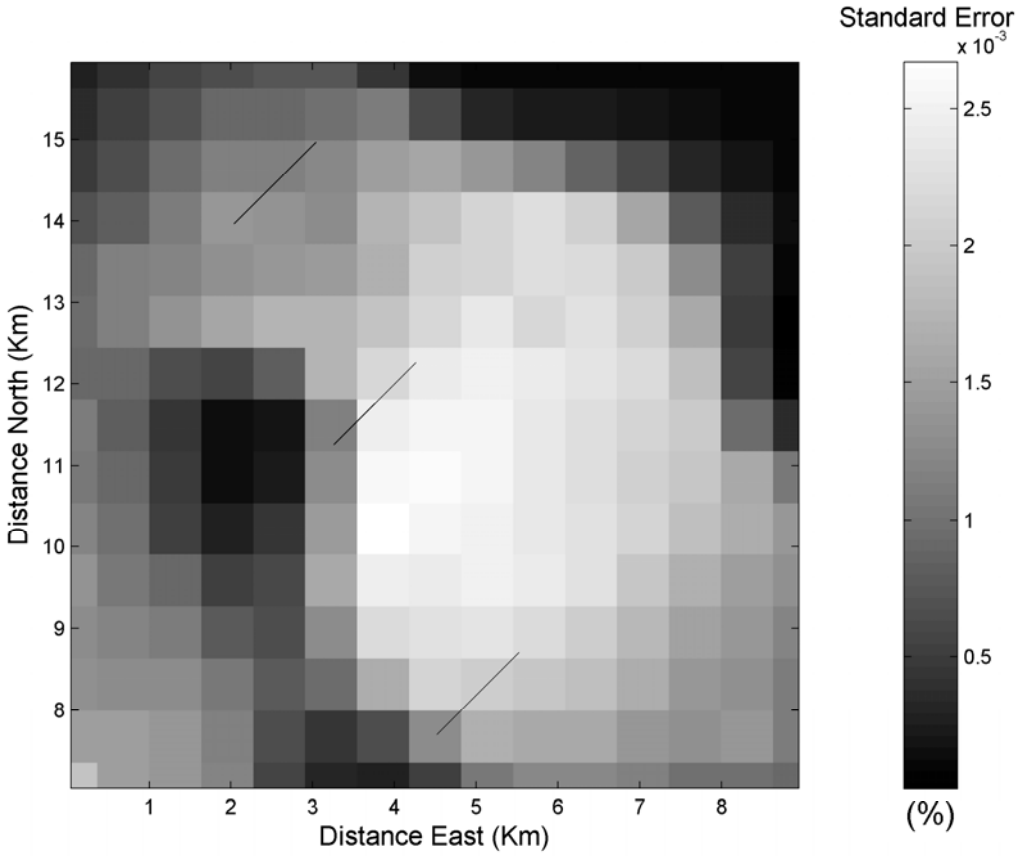
Standard Error
x 10^-3
2.5
2
1.5
1
0.5
(%)
Distance North (Km)
15
14
13
12
11
10
9
8
1
2
3
4
5
6
7
8
Distance East (Km)

Figure 13

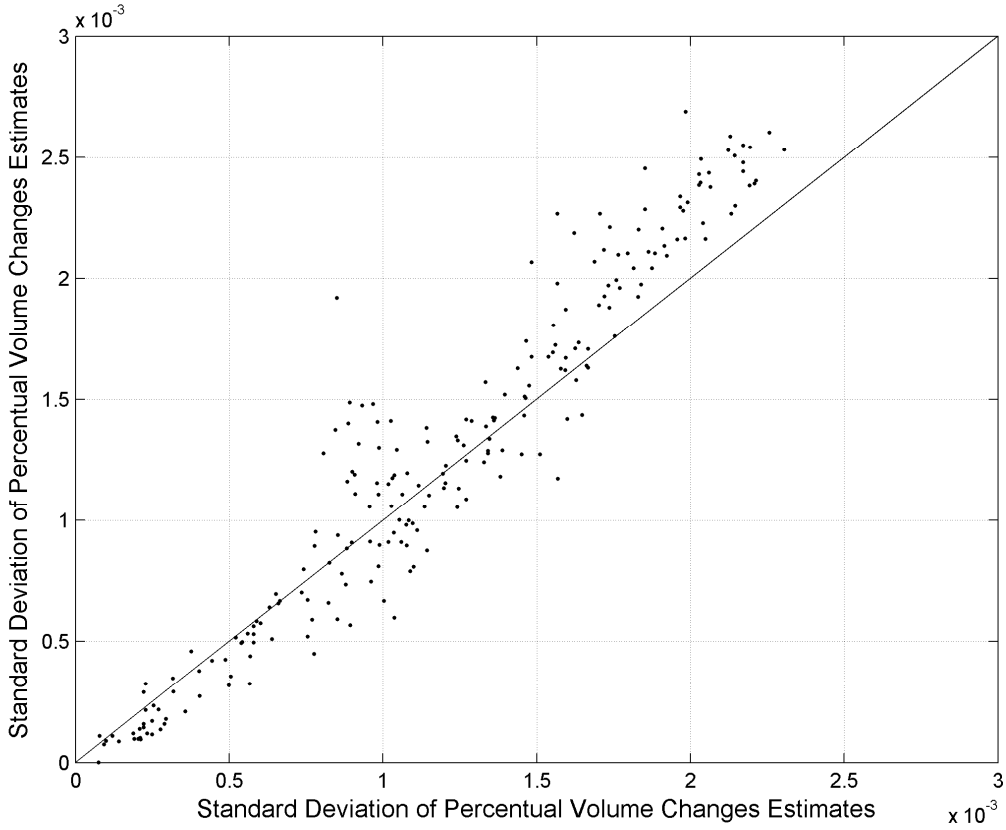
x 10^-3
3
2.5
2
1.5
1
0.5
0
Standard Deviation of Percentual Volume Changes Estimates
0
0.5
1
1.5
2
2.5
3
Standard Deviation of Percentual Volume Changes Estimates
x 10^-3

Figure 14

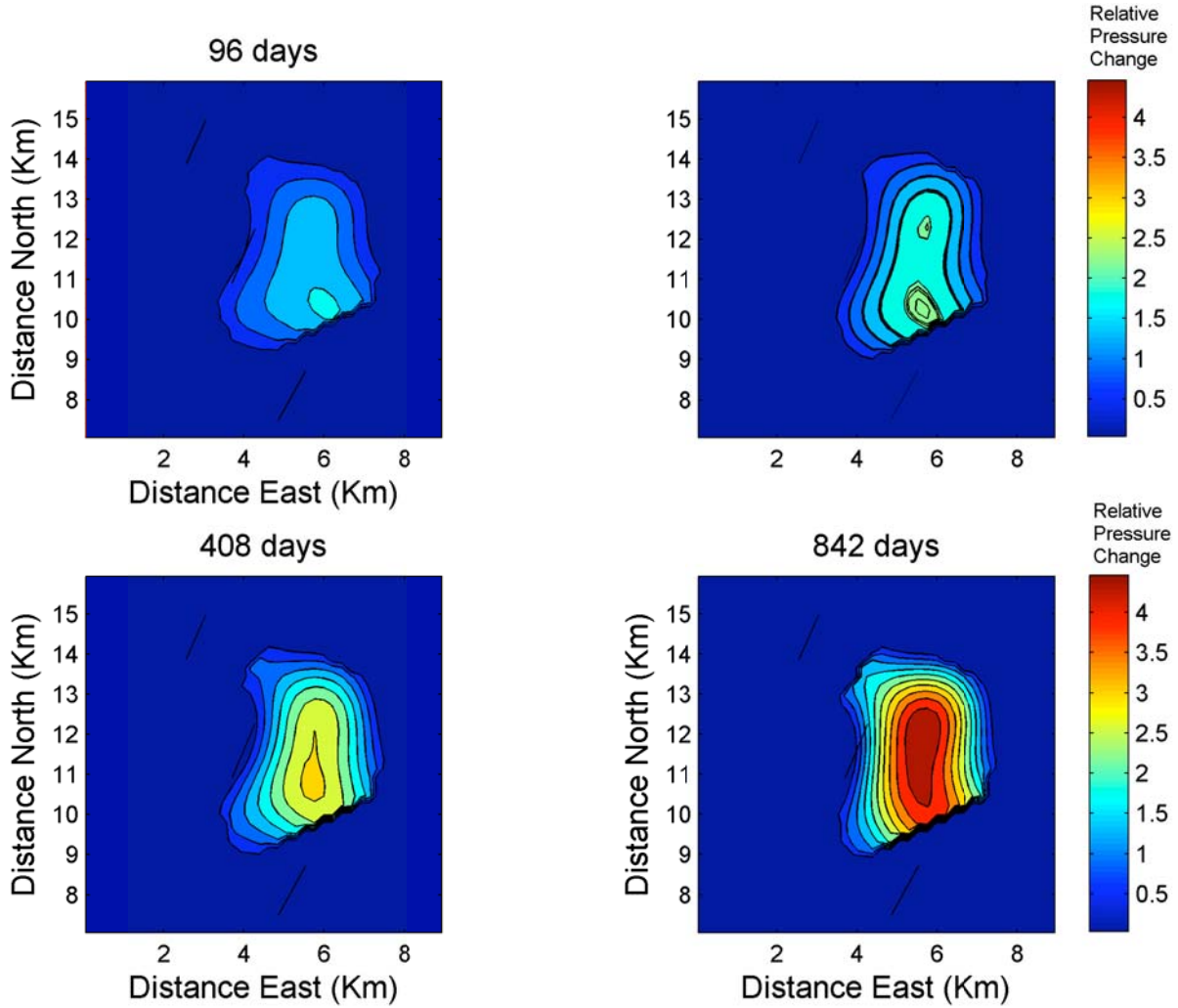
96 days
408 days
842 days
Distance North (Km)
Distance East (Km)
Relative Pressure Change
15
14
13
12
11
10
9
8
2
4
6
8
4
3.5
3
2.5
2
1.5
1
0.5

Figure 15

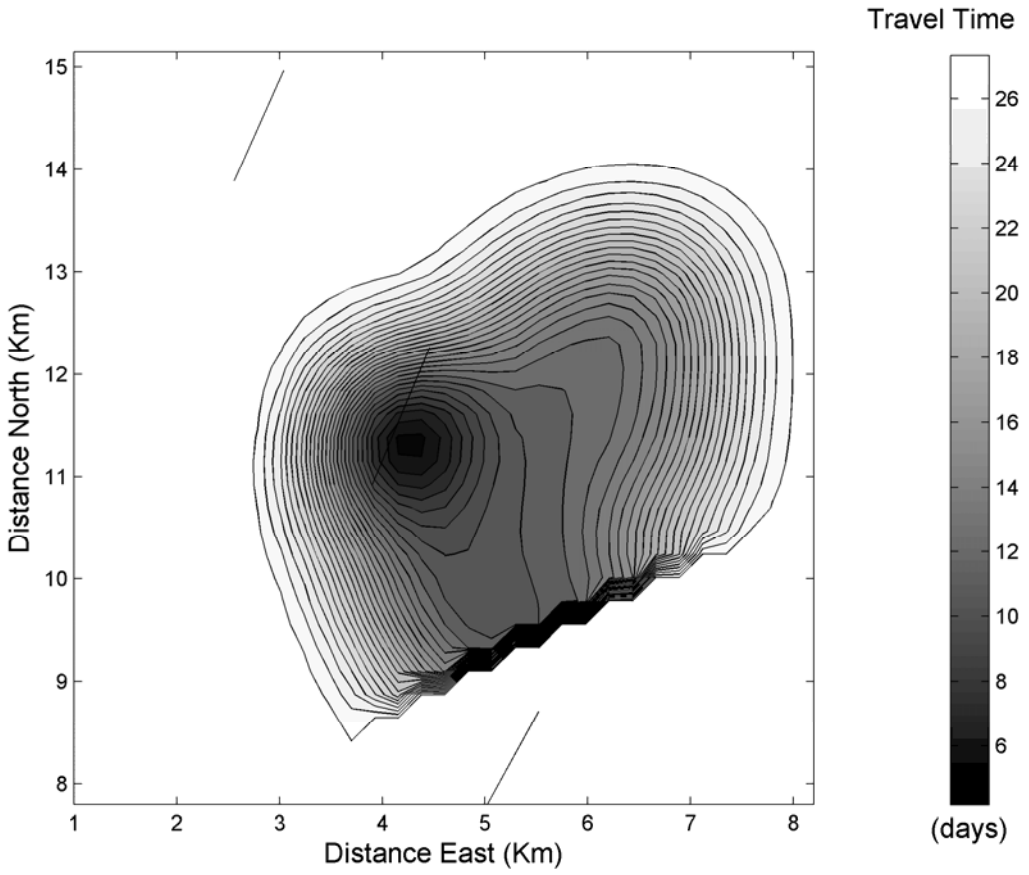
Travel Time
Distance North (Km)
Distance East (Km)
(days)
15
14
13
12
11
10
9
8
1
2
3
4
5
6
7
8
26
24
22
20
18
16
14
12
10
8
6

Figure 16

96 days
198 days
408 days
842 days
Distance North (Km)
Distance East (Km)
Relative Pressure Change
15
14
13
12
11
10
9
8
2
4
6
8
0.5
1
1.5
2
2.5
3
3.5
4

Figure 17

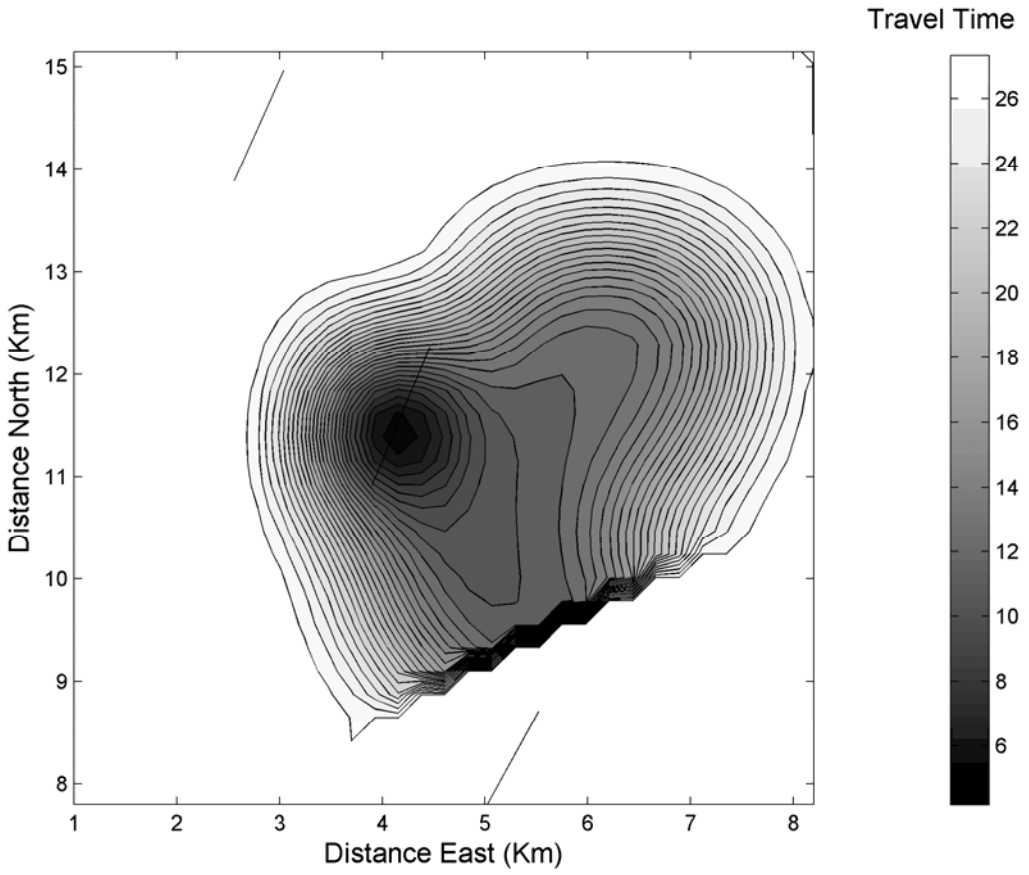
Travel Time
26
24
22
20
18
16
14
12
10
8
6
Distance North (Km)
15
14
13
12
11
10
9
8
1
2
3
4
5
6
7
8
Distance East (Km)

Figure 18

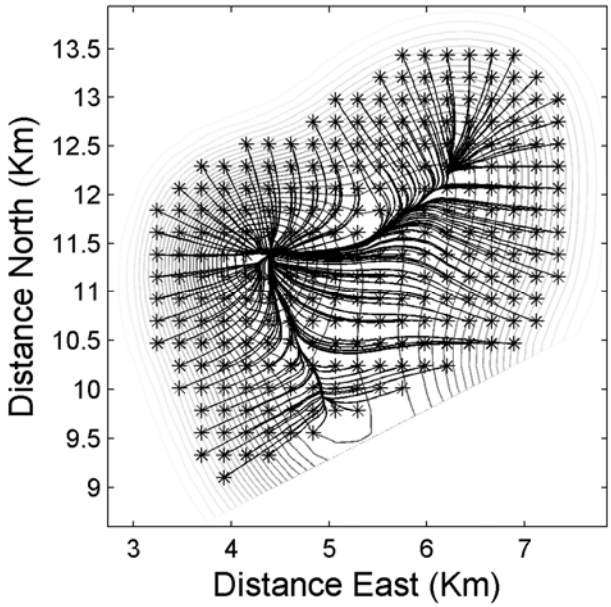
Distance North (Km)
13.5
13
12.5
12
11.5
11
10.5
10
9.5
9
3
4
5
6
7
Distance East (Km)

Figure 19

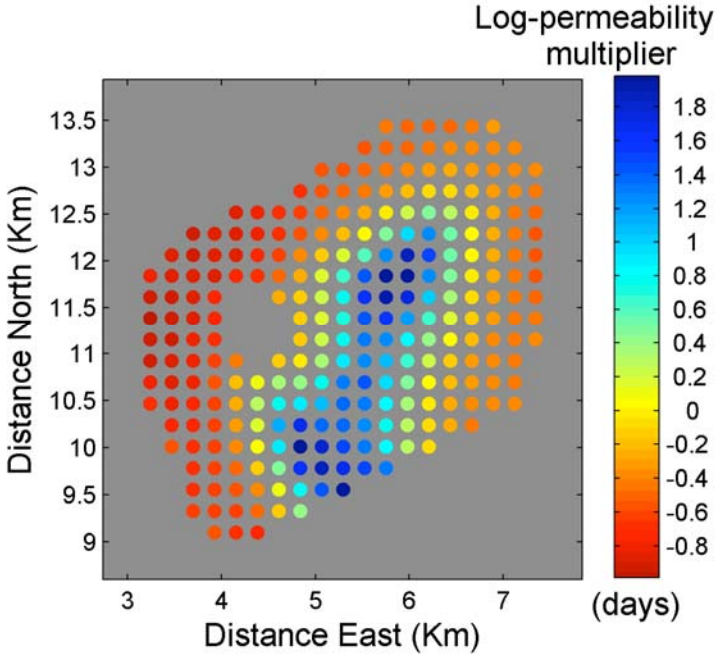
Log-permeability
multiplier
1.8
1.6
1.4
1.2
1
0.8
0.6
0.4
0.2
0
-0.2
-0.4
-0.6
-0.8
(days)
Distance North (Km)
13.5
13
12.5
12
11.5
11
10.5
10
9.5
9
3
4
5
6
7
Distance East (Km)

Figure 20